



HAL
open science

Impact of the lateral blast on the spatial pattern and grain size characteristics of the 18 May 1980 Mount St. Helens fallout deposit

Julia Eychenne, Katharine Cashman, Alison Rust, Adam Durant

► To cite this version:

Julia Eychenne, Katharine Cashman, Alison Rust, Adam Durant. Impact of the lateral blast on the spatial pattern and grain size characteristics of the 18 May 1980 Mount St. Helens fallout deposit. *Journal of Geophysical Research: Solid Earth*, 2015, 120 (9), pp.6018-6038. 10.1002/2015JB012116 . hal-03854975

HAL Id: hal-03854975

<https://uca.hal.science/hal-03854975>

Submitted on 16 Nov 2022

HAL is a multi-disciplinary open access archive for the deposit and dissemination of scientific research documents, whether they are published or not. The documents may come from teaching and research institutions in France or abroad, or from public or private research centers.

L'archive ouverte pluridisciplinaire **HAL**, est destinée au dépôt et à la diffusion de documents scientifiques de niveau recherche, publiés ou non, émanant des établissements d'enseignement et de recherche français ou étrangers, des laboratoires publics ou privés.

RESEARCH ARTICLE

10.1002/2015JB012116

Key Points:

- The co-blast plume enriched the Mount St. Helens fallout deposit in fine ash
- Fine ash settled by a combination of enhanced sedimentation mechanisms
- A significant proportion of the Mount St. Helens fallout deposit is nonjuvenile

Supporting Information:

- Tables S1 and S2
- Data Set S1
- Data Set S2
- Data Set S3
- Data Set S4
- Data Set S5
- Data Set S6

Correspondence to:

J. Eychenne,
julia.eychenne@bristol.ac.uk

Citation:

Eychenne, J., K. Cashman, A. Rust, and A. Durant (2015), Impact of the lateral blast on the spatial pattern and grain size characteristics of the 18 May 1980 Mount St. Helens fallout deposit, *J. Geophys. Res. Solid Earth*, 120, 6018–6038, doi:10.1002/2015JB012116.

Received 13 APR 2015

Accepted 1 AUG 2015

Accepted article online 6 AUG 2015

Published online 4 SEP 2015

Impact of the lateral blast on the spatial pattern and grain size characteristics of the 18 May 1980 Mount St. Helens fallout deposit

Julia Eychenne¹, Katharine Cashman¹, Alison Rust¹, and Adam Durant^{2,3}

¹School of Earth Sciences, University of Bristol, Bristol, UK, ²Section for Meteorology and Oceanography, Department of Geosciences, University of Oslo, Oslo, Norway, ³Geological and Mining Engineering and Sciences, Michigan Technology University, Houghton, Michigan, USA

Abstract The 18 May 1980 eruption of Mount St. Helens started with a lateral blast that fed a pyroclastic surge, which then uplifted to form a co-blast plume. Thirty minutes later, Plinian activity started at the vent and fluctuated in intensity for ~9 h. The resulting fallout deposit, documented to > 600 km from vent, presents some striking features: (1) displacement of the overall deposit to the north of the vent, (2) a secondary thickness and mass maximum at ~300 km from vent, (3) a total grain size distribution dominated by fine ash (62 wt % of the deposit < 63 μm), and (4) individual grain size distributions that vary dramatically in the crosswind direction from strongly bimodal in the south to skewed unimodal in the north. Results from a new deconvolution of the individual grain size distributions show that they are a combination of a coarse subpopulation that decreases in size with distance from vent and a constant fine subpopulation with a mean of ~15 μm. Relative proportions of each subpopulation vary asymmetrically in the crosswind directions, with the fine subpopulation preponderant toward the north and the coarse one dominating the south of the deposit, both reach their absolute maxima in mass on the deposit axis. Componentry analyses of selected samples show that blast-derived material is greatly enriched toward the north of the deposit. These results indicate that the co-blast plume dispersed fine-grained material over great distances and dominated the fine subpopulation. Comparison with reanalysis data of atmospheric wind fields and satellite images of the spreading ash cloud suggests contrasting ash transport and depositional processes for the (early) co-blast plume and the (later) vent-derived Plinian plumes. The co-blast plume is displaced to the north; it had a high overshoot height, and eastward dispersion via strong winds low in the stratosphere (~10–15 km). The Plinian plumes were lower and dispersed most of the material to the southeast as the direction of high-velocity winds shifted just before the late climactic Plinian eruptive phase. Fine ash (fine subpopulation) was deposited continuously throughout the deposit, with an increase of sedimentation rate ~300 km from the vent where there is a secondary maximum in the deposit mass and thickness. Fine ash probably settled by a combination of enhanced sedimentation mechanisms, including not only aggregation but also gravitational convective instabilities of cloud base, hydrometeor formation and destruction, and entrainment of small particles by larger ones. Finally, we show that half of the deposit (by mass) in the medial area was deposited by the co-blast plume, and that a significant proportion of the Mount St. Helens fallout deposit is nonjuvenile, which has implications for the magmatic budget of this eruption.

1. Introduction

The 18 May 1980 eruption of Mount St. Helens (USA) was a key event for the development of modern volcanology and has produced major scientific advances regarding the dynamics of explosive eruptions. In particular, many concepts underpinning our understanding of ash transport and deposition from volcanic plumes stem from insights gained from the extraordinary quality of the field observations, including both field measurements and remote sensing data collected during and after the event. One example is the commonly accepted theory that distal mass accumulation maxima in tephra fall deposits are the signature of premature fallout of fine material due to aggregation [Brown *et al.*, 2012; Durant and Rose, 2009], which was first developed to explain the depositional pattern of the 18 May 1980 Mount St. Helens fallout [e.g., Carey and Sigurdsson, 1982]. Also, groundbreaking was the exceptional characterization of ash transport: the 18 May 1980 Mount St. Helens eruption cloud was one of the first to be observed by airborne remote sensing methods (i.e., radar and satellite imagery) [Harris *et al.*, 1981; Holasek and Self, 1995; Rice, 1981;

Sparks et al., 1986] and sampled in situ by research aircraft [*Hobbs et al.*, 1981, 1982; *Farlow et al.*, 1981]. The measured airborne grain size distribution has become one of the references for the grain size distribution input for the London Volcanic Ash Advisory Centre ash dispersion model used operationally today [*Beckett et al.*, 2014]. Finally, the tephra fall deposit is one of the most extensively mapped and sampled modern fallout deposits, with quantitative field data up to distances > 700 km from vent [*Carey et al.*, 1990; *Carey and Sigurdsson*, 1982; *Sarna-Wojcicki et al.*, 1981]. As a result of the quality of both airborne and ground observations, this eruption has been used to benchmark several generations of numerical models of ash dispersion and sedimentation [*Armienti et al.*, 1988; *Fero et al.*, 2008; *Folch et al.*, 2010; *Mastin et al.*, 2009]; the total grain size distribution is also used as input for simulations of much larger eruptions [*Mastin et al.*, 2014].

Accurate forecasts of atmospheric ash quantities are required during volcanic crises to safely manage flight operations because of the recognized impact of ash ingestion into airplane engines [*Casadevall et al.*, 1996; *Gislason et al.*, 2011; *Kueppers et al.*, 2014]. Aircraft operators require not only predictions of ash cloud transport but also, most importantly, ash concentration to anticipate potential airspace closures [*Beckett et al.*, 2014; *Witham et al.*, 2007]. One consequence of these new requirements is the need for accurate input data to initialize both operational numerical models for ash dispersion [*Mastin et al.*, 2009; *Stohl et al.*, 2011] and algorithms for ash retrieval from satellite images [*Guéhenneux et al.*, 2015; *Labazuy et al.*, 2012; *Mackie and Watson*, 2014]. Discrepancies between predictions of ash dispersion (spatial distribution, concentration, and grain size) and ash measured and sampled on the ground during recent volcanic crises [*Stevenson et al.*, 2015] have highlighted the limitations of the commonly used eruption source parameters. Further problems come from modeling the sink term used to forecast volcanic ash cloud transport, which is not accurately represented in operational models and may thus overestimate far-field airborne ash quantities [*Durant*, 2015]. Especially critical are (1) the initial grain size distribution and (2) the mass eruption rate. The former is generally approximated using total grain size distributions from known eruptions (for proximal dispersion) [*Bonadonna et al.*, 2015; *Bonadonna and Houghton*, 2005] and airborne (in situ) measurements of grain sizes (for distal clouds) [*Flentje et al.*, 2010; *Hobbs et al.*, 1981, 1982; *Johnson et al.*, 2012]. The latter is derived from the column height by an empirical law with a theoretical basis [*Degruyter and Bonadonna*, 2012; *Mastin et al.*, 2009; *Sparks et al.*, 1997; *Woodhouse et al.*, 2013]. Yet recent work has shown that both the dispersion of volcanic eruption clouds and sedimentation of ash from those clouds are spatially and temporally complex because of gravitational instabilities of the cloud base [*Carazzo and Jellinek*, 2012; *Carazzo and Jellinek*, 2013; *Chakraborty et al.*, 2006; *Manzella et al.*, 2015], ice nucleation on ash particles and formation of hydrometeors [*Bingemer et al.*, 2012; *Durant*, 2015; *Durant et al.*, 2009, 2008], and the variety and time dependence of aggregation processes [*Brown et al.*, 2012]. Furthermore, the addition of fine ash transported in plumes uplifting from pyroclastic density currents (PDCs) during their propagation [*Andrews and Manga*, 2012; *Bonadonna et al.*, 2002; *Sparks and Walker*, 1977], hereafter generically referred to as co-PDC plumes, will affect the grain size, mass, and energetics of the dispersing plume and yet has rarely been accounted for in plume models.

In light of these new findings and to investigate the role and impact of co-PDC plumes on ash transport during a well-documented modern eruption, we return to the iconic eruption of Mount St. Helens to reexamine and decipher its distal fallout deposit. Despite being a “textbook” case of a Plinian eruption, the 18 May 1980 eruption of Mount St. Helens had unusual dynamics and produced a complex fallout deposit. In addition to its remarkable secondary thickness maximum ~300 km from the vent, the fallout deposit presents several striking features. First, the overall deposit is displaced to the north of the vent [*Carey and Sigurdsson*, 1982; *Sarna-Wojcicki et al.*, 1981], a feature that has yet to be included in ash dispersion models except by moving the presumed vent for the entire eruption to the north [*Armienti et al.*, 1988; *Fero et al.*, 2008; *Folch et al.*, 2010]. Second, the total grain size distribution, which contains 62% by mass of fine ash (<63 μm), makes it one of the most fine-rich fallout deposits ever characterized [*Rust and Cashman*, 2011]. Finally, individual grain size distributions vary dramatically not only downwind but also in the crosswind direction [*Durant et al.*, 2009]. These features have never been satisfactorily reproduced by numerical models of plume dispersion [*Armienti et al.*, 1988; *Fero et al.*, 2008; *Folch et al.*, 2010] except by using effective grain sizes (and settling velocities) back calculated from the deposit data [*Hopkins and Bridgman*, 1985].

To reexamine key features of the deposit, we use a new method to deconvolve individual grain size distributions and combine these data with componentry analyses of selected crosswind and downwind samples. We then compare the field observations with reanalysis data of the atmospheric wind field, satellite images of the

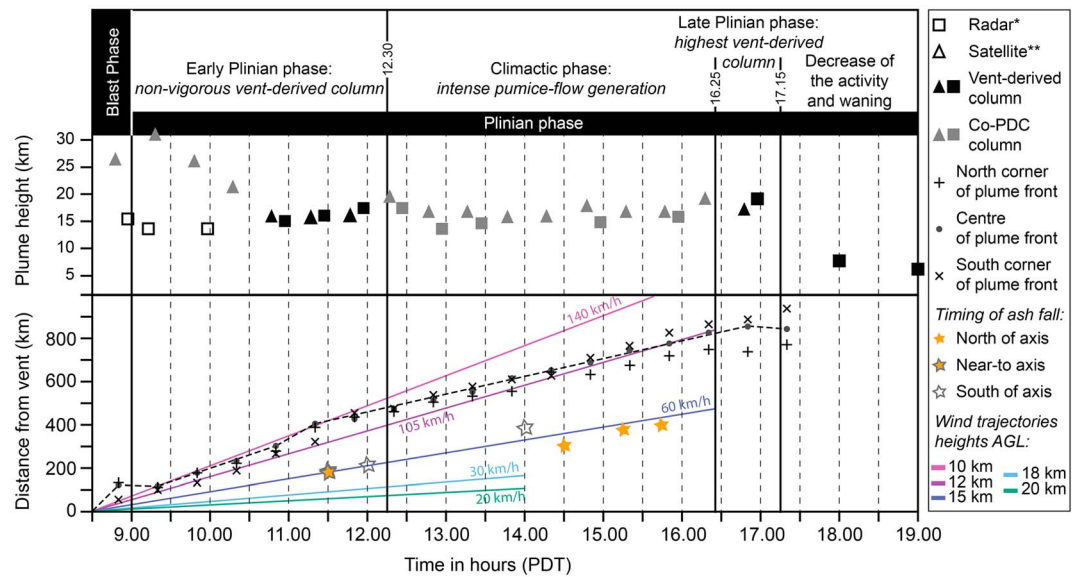


Figure 1. Summary of the eruptive activity at the vent and of the plume dispersal throughout the duration of the eruption. The nature of the plumes (i.e., vent derived versus co-PDC) along with the timing and definition of the eruptive phases was inferred by cross-correlating plume height measurements, observations from the ground, and interpretations from the literature [Carey et al., 1990; Criswell, 1987; Sparks et al., 1986]. The extent of the dispersing plume toward the east was measured on the isochrone map built from the GOES visible images in Holasek and Self [1995]. Asterisk: Plume heights estimated using radar observations from Portland, Oregon [Harris et al., 1981]. Double asterisks: Plume heights retrieved from GOES visible satellite images using the shadow method [Holasek and Self, 1995]. The locations where timing of ash settling was observed are shown in Figure 2, with references detailed in caption. The colored straight lines in the bottom diagram represent eastward wind trajectories at different heights (calculated using HYSPLIT, see Figure 9). The labels indicate the wind velocity.

spreading ash cloud, and the timing of the first ash fall at various distances from the volcano. Our results highlight the complex interaction between the co-PDC plume formed by the blast and the later vent-derived plumes from the Plinian phase and emphasize, particularly, the ultimate impact of the blast on the characteristics of the fallout deposit.

2. Background

2.1. 18 May 1980 Mount St. Helens Eruption: Chronology

The chronology of the 18 May 1980 Mount St. Helens eruption has been well constrained by combining information from eye witness accounts [Criswell, 1987; Rosenbaum and Waitt, 1981], photographs and videos [Hoblitt, 2000; Moore and Rice, 1984; Voight, 1981], stratigraphic studies of the proximal deposits [Criswell, 1987; Hoblitt et al., 1981; Rowley et al., 1981; Sarna-Wojcicki et al., 1981; Waitt and Dzurisin, 1981], and radar and satellite observations of the ash plumes [Harris et al., 1981; Holasek and Self, 1995; Sparks et al., 1986]. The eruption started at 08:32 in the morning (Pacific Daylight Time, PDT) with a catastrophic collapse of the northern flank of the volcano, which triggered the decompression of a shallow cryptodome and caused a blast directed toward the north that was accompanied by only a small (<8 km above sea level (asl)) vertical plume at the vent [Glicken, 1990; Hoblitt, 2000; Moore and Rice, 1984]. The blast generated a pyroclastic surge that covered an area of 572 km² to the north of the volcano in ~5 min [Druitt, 1992; Hoblitt et al., 1981; Moore and Sisson, 1981]. It then uplifted abruptly at 10–15 km north of the vent and fed a huge convective column and plume that reached a maximum height of 30 km [Holasek and Self, 1995; Sparks et al., 1986]. This blast-derived co-PDC plume (hereafter referred as co-blast plume) then dispersed toward the east, following the prevailing atmospheric winds (Figure 1) [Holasek and Self, 1995].

The Plinian phase started soon after 09:00 and formed a weak to moderate vertical column at the vent that reportedly fluctuated around ~14 km height for the next 3 h [Criswell, 1987; Harris et al., 1981]. Curiously, this column is not evident in the GOES satellite images presented by Holasek and Self [1995]. Eruptive activity

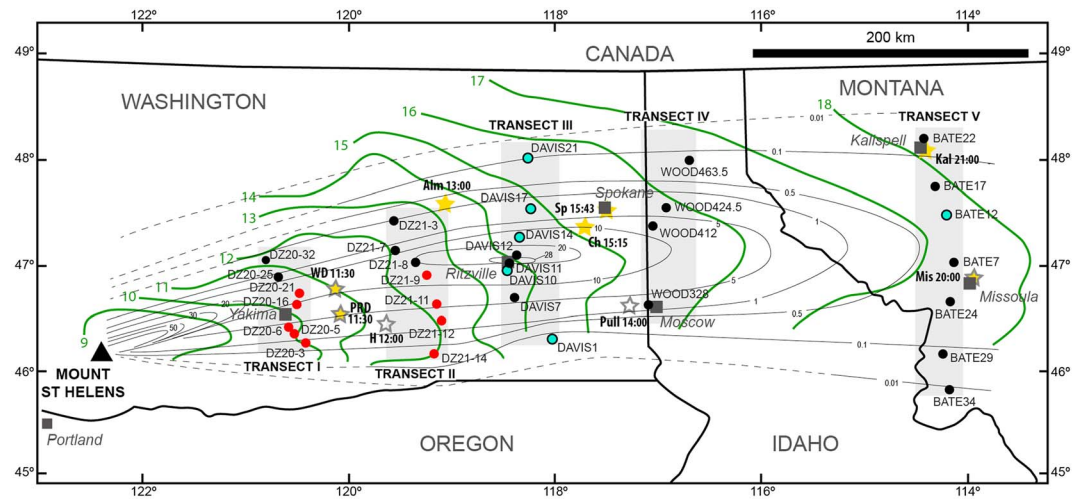


Figure 2. Map of the 18 May 1980 Mount St. Helens fallout deposit picturing the isomass lines drawn by *Sarna-Wojcicki et al.* [1981] in kg/m² (thin grey contours). The dots represent the locations of samples considered in this study. Red dots are samples with bimodal grain size distributions; dots with blue cores are the samples studied for componentry. Shaded zones define the five north-south transects of samples referred to in the text. Green lines are isochrones of first ash fall (Pacific Daylight Time) from *Quinn* [1982]. Stars represent independent observations of first ashfall at specific locations, also reported in Figure 1 (Pacific Daylight Time). Data are from *Scheidegger et al.* [1982] (WD, PRD, and H), *Hooper et al.* [1980] (Pull), *Ikramuddin et al.* [1982] (Ch), *Stoiber et al.* [1981] (Alm), and *Sarna-Wojcicki et al.* [1981] (Sp, Mis, Kal).

during this time period generated only a few small PDCs that were emplaced on the upper flanks of the volcano [Carey et al., 1990; Criswell, 1987]. Vigorous PDC activity started around 12:15 and was accompanied by vertically distributed earthquakes that recorded full connection of the deeper magma storage region to the surface [Scandone et al., 2007]. Activity increased in intensity again between 15:00 and 16:00; resulting pumice flows on the north flank had a typical runout distance of 8 km [Rowley et al., 1981] and produced co-PDC plumes with an elongated source that extended 4–7 km north of the crater [Carey et al., 1990; Criswell, 1987]. At 16:25, activity changed with the formation of a vertical column from the vent [Criswell, 1987] that reached a maximum height of 20 km before dropping to 6 km at 18:00 [Harris et al., 1981; Holasek and Self, 1995] as the eruption progressively waned (Figure 1). The different plumes related to the Plinian activity all dispersed toward the east with the prevailing winds [Holasek and Self, 1995].

2.2. 18 May 1980 Mount St. Helens Eruption: Eruptive Products

The eruptive products associated with the two phases of the eruption (blast and Plinian) are very distinctive. Material from the blast phase originated from the volcanic edifice, the cryptodome, and the upper part of the conduit; as a result, the juvenile component was degassed and microlite rich (abundant plagioclase laths surrounded in places by poikilitic quartz) [Cashman and Hoblitt, 2004; Hoblitt and Harmon, 1993]. This material has a dacitic bulk composition with a highly evolved glass (>79 wt % SiO₂ measured in the most crystalline samples) [Blundy and Cashman, 2001] and ~30% phenocrysts [Cashman and Taggart, 1983]. Large volumes of variably fragmented material from the collapsed edifice were also ejected during this early phase [Druitt, 1992; Hoblitt and Harmon, 1993].

The Plinian phase, in contrast, primarily erupted highly vesicular and microlite-poor pumice and ash [Klug and Cashman, 1994] created during rapid ascent of magma from a storage system at intermediate depth (6 to 12 km) [Scandone et al., 2007]. The Plinian material had a dacitic bulk composition (63 wt % SiO₂), with a rhyolitic matrix glass (73 wt % SiO₂), and ~30% phenocrysts of amphibole, plagioclase, orthopyroxene, Fe-Ti oxides, and rare clinopyroxene [Blundy and Cashman, 2001; Kuntz et al., 1981; Rutherford et al., 1985].

2.3. 18 May 1980 Mount St. Helens Eruption: Fallout Deposit

The eruption produced a widespread fall deposit that extended across the states of Washington, Idaho, and Montana; the observed plume reached a maximum width of 200 km and extended east for > 600 km before drifting south. The signature characteristic of the fall deposit is a secondary thickness and mass maximum

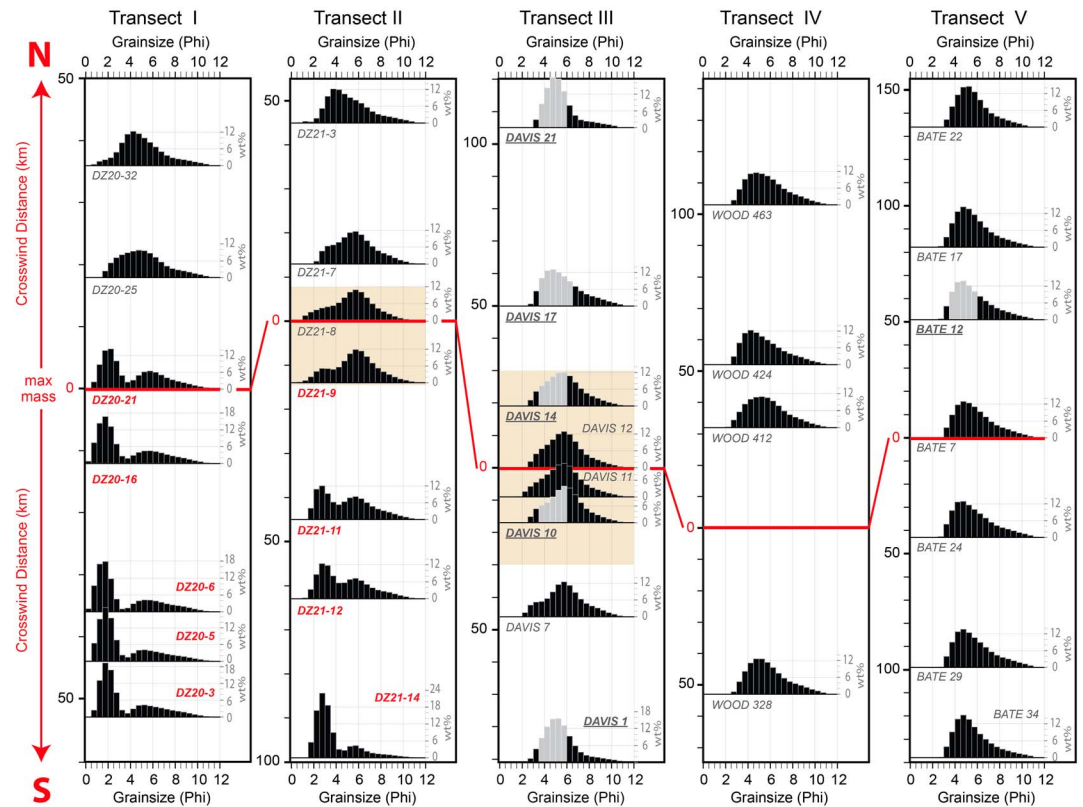


Figure 3. GSDs of 33 samples from the 18 May 1980 Mount St Helens fallout deposit, as analyzed by *Durant et al.* [2009]. Distributions are organized by transects (Figure 2) and plotted vertically at their projected distance (in km) from the deposit axis, represented by the red horizontal line (location of maximum deposited mass). Note that the vertical distance axis has a different scale for each transect. Samples with bimodal grain size distributions labeled in red; secondary thickness maximum highlighted by brown boxes. Samples analyzed for componentry are underlined; approximate range of grain sizes analyzed is represented by grey histogram bars. All GSDs plotted on same scale.

that represents an overthickening of ~30 mm at about 300 km from vent [*Carey and Sigurdsson, 1982; Sarna-Wojcicki et al., 1981*] (Figure 2). Other curious features are the apparent northward displacement of the overall deposit relative to the vent and a shift of the deposit axis from the ENE to E at a distance of ~200 km. Although these latter aspects of the fall deposit have never been discussed explicitly, all published attempts to model the deposit have required that the vent source be displaced tens of kilometers north of the mountain [*Armienti et al., 1988; Fero et al., 2008; Folch et al., 2010*].

The proximal fall deposit (20–60 km downwind) comprised a succession of four stratigraphic units that varied in grain size, juvenile type, and lithic content [*Criswell, 1987; Waitt and Dzurisin, 1981*]. Between 100 and 550 km from vent, only two layers were identified: a basal light grey layer of fine ash up to 20 mm thick and an upper light grey to tan layer of ash accounting for the rest of the thickness [*Sarna-Wojcicki et al., 1981*]. This change in color was interpreted to correspond to the color change of the vent-derived plume at 12:15, which heralded the onset of ubiquitous PDC activity [*Criswell, 1987; Sarna-Wojcicki et al., 1981*]. Yet there is no documentation of a change in grain size or componentry associated with the change in color in the deposit [*Scheidegger et al., 1982*]. Beyond 550 km, the deposit comprised only a single light grey layer of fine ash [*Sarna-Wojcicki et al., 1981*].

Reconstructions of the total grain size distribution (TGSD) reveal a deposit dominated by fine material (62 wt % of the deposit finer than 63 μm) [*Durant et al., 2009*], which is at the fine-grained extreme of TGSDs from well-documented explosive eruptions [*Rust and Cashman, 2011*]. The grain size distributions of 33 samples collected by U.S. Geological Survey scientists during the days immediately following the eruption [*Sarna-Wojcicki et al., 1981*] were reanalyzed by *Durant et al.* [2009] to remeasure, in particular, the smallest particles by laser diffraction methods. These samples come from five N-S transects that lie roughly perpendicular to the deposit axis and

span from 160 to 630 km from the vent (Figure 2). The data are remarkable not only in the extent to which individual samples depart from a lognormal shape (from bimodal in transects I and II to strongly skewed in transects IV and V) but also in the systematic change in grain size distributions (GSD) shape from south (bimodal) to north (unimodal) along individual crosswind transects (Figure 3).

By averaging GSDs along each transect, *Durant et al.* [2009] demonstrated a global decrease of the mean diameter and an improvement of the sorting from transects I to V, consistent with size fractionation during ash dispersion and sedimentation from the plume [*Bursik et al.*, 1992; *Fisher*, 1964; *Sparks et al.*, 1992]. By deconvolving individual GSDs, they also identified a subpopulation (average mode 19 μm) that reaches a maximum proportion in transect III (320 km from the vent), which crosses the secondary maximum at Ritzville (Figure 2). Consistent with earlier workers, they interpreted this subpopulation to record enhanced sedimentation by ash aggregation; they provided a new mechanism for aggregation, however, by suggesting that the timing of aggregation and fallout was controlled by hydrometeor formation as the particle-laden clouds descended through the ice melting point (at ~ 7 km altitude).

Hydrometeor formation, however, does not explain the extraordinary GSD variations along transects I, II, and III (Figure 3), which have not been addressed by any previously published studies. Transects I and II (at 160 and 250 km from vent, respectively) are particularly noteworthy in this regard, in that strongly bimodal GSDs toward the southern edge of the deposit transform dramatically to unimodal fine-grained distributions toward the north. Along transect III (through the maximum of the secondary thickness isopachs), GSDs from samples on the deposit edges (DAVIS1 and DAVIS 21) are quasi-lognormal, but GSDs across the secondary thickening axis also transition from pseudobimodal in the south to skewed unimodal in the north.

2.4. Deconvolving Grain Size of Fallout Deposits

Detailed studies of the grain size of fallout deposits have proved critical for deciphering both source fragmentation processes [*Kaminski and Jaupart*, 1998; *Kueppers et al.*, 2006] and the dynamics of eruptive columns and dispersing plumes [*Carey and Sparks*, 1986; *Koyaguchi*, 1994]. Analysis of individual GSDs within fall deposits provides further information on mechanisms of transport and pyroclast sedimentation, which alter the source grain size distribution [*Fisher*, 1964; *Pyle*, 1989] by fractionation processes related to contrasting settling and flow behaviors of particles of different size and density.

The GSD of a pyroclastic deposit sample can be quantified by a probability density function, which is typically obtained by combining sieving ($>90 \mu\text{m}$) and laser diffraction ($<90 \mu\text{m}$) analyses [*Eychenne et al.*, 2012]. GSDs from fallout deposits are often complex, sometimes polymodal, and rarely follow an obvious mathematical function [*Folk*, 1966; *Wohletz et al.*, 1989]. In an attempt to reconcile the grain size of pyroclastic deposits with theory of fragmentation and transport, *Wohletz et al.* [1989] developed a model to deconvolve complex grain size distributions (those that depart from a lognormal shape) into sets of lognormal subpopulations. Although initially developed to study sequential fragmentation during transport in PDCs, this approach has been broadly applied to tephra fall deposits [e.g., *Durant and Rose*, 2009; *Durant et al.*, 2009; *Taddeucci and Palladino*, 2002]. Importantly, this approach commonly generates more subpopulations than observed distribution modes. Additionally, there is little evidence that either primary or secondary fragmentation processes produce lognormal grain size distributions [*Rust and Cashman*, 2011].

Eychenne et al. [2012] developed an alternative method to deconvolve polymodal distributions that limits the number of subpopulations to the number of identifiable modes in the raw distribution and does not assume that the subpopulations are necessarily lognormal. Instead, this method uses the versatile Weibull function, which can reproduce the shape of many probability density functions (e.g., lognormal, Gaussian, and Rayleigh distributions).

3. Methodology

Here we reexamine two aspects of the Mount St. Helens fallout deposit. First, we reanalyze the grain size data of *Durant et al.* [2009] using methods developed by *Eychenne et al.* [2012]. Second, we use scanning electron microscope images to identify individual components of samples collected both across the secondary thickness maximum and in one distal location. Together, these analyses provide important new insight into the origin of the fallout deposit.

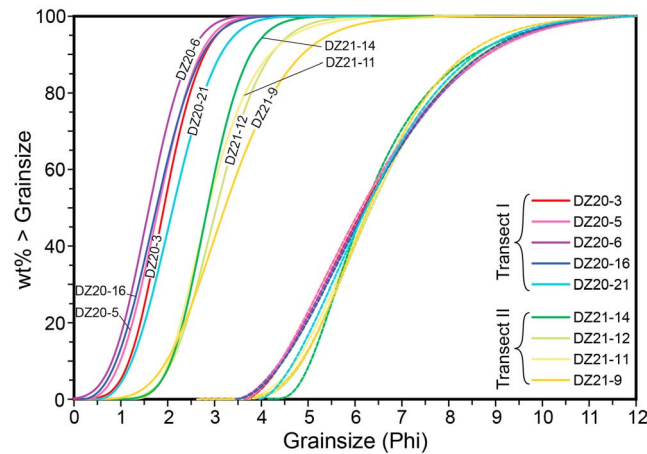


Figure 4. Cumulative density functions of the deconvolved grain size subpopulations (using DECOLOG 5.0) for the samples with bimodal GSDs (see Figure 3). Solid lines represent the coarse subpopulations, and dashed lines the fine subpopulations.

ation that varies in both shape and mode (Figure 4). These two subpopulations will be hereafter referred to as CS_b and FS_b (for “Coarse and Fine Subpopulation from bimodal samples,” respectively). The probability density functions of the FS_bs were fitted by a Weibull function using a nonlinear regression algorithm of the form

$$f(x) = \frac{a}{b} \left(\frac{x-c}{b}\right)^{a-1} \exp\left[-\left(\frac{x-c}{b}\right)^a\right], \quad (1)$$

where x is the grain size in $\Phi = -\log_2$ (grain size in mm), a is a constant controlling the shape of the distribution (from positively to negatively skewed to Gaussian), b is a constant controlling the spread of the distribution along the abscissa, and c is a constant controlling the location of the distribution along the abscissa. The parameters obtained are summarized in Table S1 of the supporting information.

To assess whether the remaining 24 unimodal distributions could also be described by a constant fine subpopulation and a varying coarse subpopulation, we developed an algorithm to deconvolve the unimodal

3.1. Processing of the Grain Size Data

Nine of the 33 samples presented in Durant et al. [2009] show bimodal GSDs (in transects I and II; Figures 2 and 3); in these samples, we separated the two distinct peaks by adapting the approach of Eychenne et al. [2012] described above. We extracted two subpopulations corresponding to the two modes of the raw bimodal GSDs using the fully automated DECOLOG 5.0 software [Bellotti et al., 2010; Caballero et al., 2014], which is based on an iterative algorithm for optimizing nonlinear fitting of Weibull functions. Initial deconvolutions suggest that the bimodal distributions contain a fine subpopulation with very similar characteristics for all the samples, and a coarse subpopula-

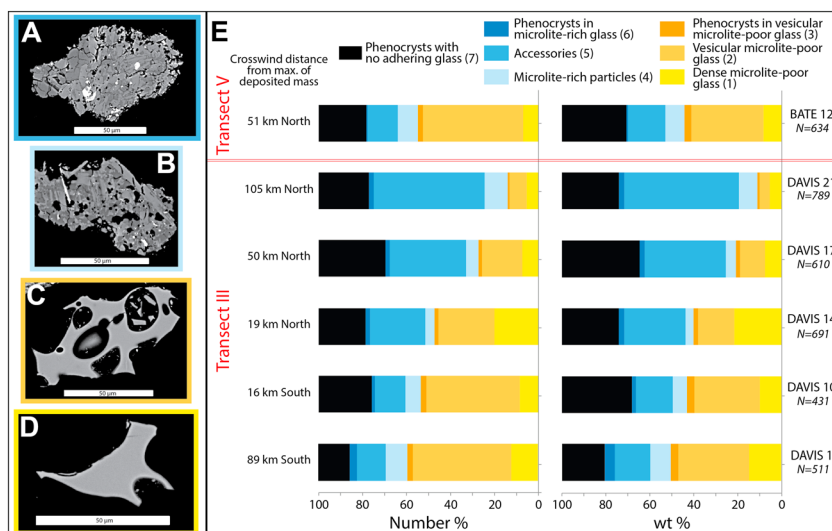


Figure 5. Examples of particles from componentry classes: (a) Accessory (5), (b) Microlite-rich particles (4), (c) vesicular microlite-poor glass (2), and (d) dense glass (1). (e) Componentry distributions in number and mass percent (see text for conversion protocol) within six samples from the fallout deposit. N is the number of particles counted. The number by the componentry class in the legend refers to component description in section 3.2.

Table 1. Mean Particle Densities Used to Convert Componentry Distributions From Number % to wt %^a

Componentry Class	Mean Particle Density (g/cm ³)	References or Assumptions
Dense microlite-free glass (1)	2.30	Cashman and McConnell [2005]
Vesicular microlite-free glass (2)	1.38	Mean vesicularity of 40%
Microlite-rich particles (4)	1.83	Hoblitt and Harmon [1993]
Accessories (5)	2.37	Hoblitt and Harmon [1993]
Crystals (3, 6, and 7)	2.60	Cashman and McConnell [2005]

^aNumbers in first column refer to componentry categories in section 3.2.

probability density functions into a fixed fine subpopulation (varying only within the range defined by the nine FS_bs) and a coarse subpopulation of unknown shape. These two subpopulations will be hereafter referred to as CS_u and FS_u (for “Coarse and Fine Subpopulation from unimodal samples,” respectively). CS_u is modeled by a Weibull function described by equation (1) with the parameters *a*, *b*, and *c* treated as unknowns. The amplitudes of CS_u and FS_u are also treated as unknowns. The algorithm allows the five unknowns to be adjusted via a graphical user interface until the

best fit is obtained. The goodness of fit is measured using the coefficient of determination (*R*²). In cases where the CS_u overlapped the FS_u by more than 70%, the deconvolution was not completed because the algorithm would not converge toward a unique solution. The mean, sorting, skewness, and kurtosis of the raw and deconvolved distributions were calculated using the method of Folk and Ward [1957]. The proportions of CS_u and FS_u within individual bulk distributions were also determined.

3.2. Componentry Analyses

Samples DAVIS1, 10, 14, 17, and 21 from transect III and sample BATE 12 from transect V (Figure 2) were also analyzed for componentry. Polished sections of resin-mounted ash < 90 μm in size (>3.5 Φ) were prepared and imaged by backscattered electrons (BSE) on a Secondary Electron Microscope (Hitachi S-3500N, School of Earth Science, University of Bristol). Seven classes of particles were distinguished in the samples (Figures 5a–5d): (1) dense angular microlite-free glass (glass shards), (2) vesicular and microlite-poor glass, (3) phenocrysts (mostly broken) included in a vesicular microlite-poor glass, (4) variably vesicular microlite-rich glass characterized by contorted vesicle shapes, (5) moderately to highly oxidized and altered accidentals of various type (holocrystalline, basalt, basaltic andesite, etc.), (6) phenocrysts (mostly broken) included in a microlite-rich glass, and (7) phenocrysts (mostly broken) without adhering groundmass. The proportions within each sample of these seven components were determined by counting particles (≥430 per sample) defined by more than 2000 pixels (~16 μm) on mosaics of BSE images. The componentry distributions in number % were converted to weight % assuming a homogeneous distribution of all the components within each analyzed grain size and a constant particle density for each individual component (Table 1). By using the mass per unit area measured in the field at the corresponding locations, we then determined the mass of each component per unit area (Table 2).

4. Results

In presenting the grain size data, we consider first the nine bimodal samples, which are found only in the two crosswind transects that are closest to the vent (I and II at 160 and 250 km, respectively). We then consider the

Table 2. Mass Per Unit Area of Different Ash Components at Locations Studied for Componentry
Mass Per Unit Area (kg/m²)

Sample	Total Sample	Dense Microlite-Free Glass	Vesicular Microlite-Free Glass	Microlite-Rich Particles	Accessor.	Pheno. in Microlite-Poor Glass	Pheno. in Microlite-Rich Glass	Pheno. Without Adhering Glass
DAVIS 1	1.8 × 10 ⁻²	2.6 × 10 ⁻³	5.7 × 10 ⁻³	1.7 × 10 ⁻³	2.9 × 10 ⁻³	6.1 × 10 ⁻⁴	8.0 × 10 ⁻⁴	3.4 × 10 ⁻³
DAVIS 10	14.7	1.5	4.4	9.5 × 10 ⁻¹	2.5	4.9 × 10 ⁻¹	2.7 × 10 ⁻¹	4.7
DAVIS 14	6.9	1.5	1.1	2.5 × 10 ⁻¹	1.9	1.4 × 10 ⁻¹	1.7 × 10 ⁻¹	1.8
DAVIS 17	9.1 × 10 ⁻¹	6.9 × 10 ⁻²	1.0 × 10 ⁻¹	4.2 × 10 ⁻²	3.4 × 10 ⁻¹	1.7 × 10 ⁻²	2.1 × 10 ⁻²	3.2 × 10 ⁻¹
DAVIS 21	6.0 × 10 ⁻³	3.3 × 10 ⁻⁴	2.8 × 10 ⁻⁴	5.0 × 10 ⁻⁴	3.1 × 10 ⁻³	6.0 × 10 ⁻⁵	1.5 × 10 ⁻⁴	1.5 × 10 ⁻³
BATE 12	1.4 × 10 ⁻¹	1.1 × 10 ⁻²	4.5 × 10 ⁻²	1.2 × 10 ⁻²	2.3 × 10 ⁻²	4.3 × 10 ⁻³	1.0 × 10 ⁻³	4.0 × 10 ⁻²

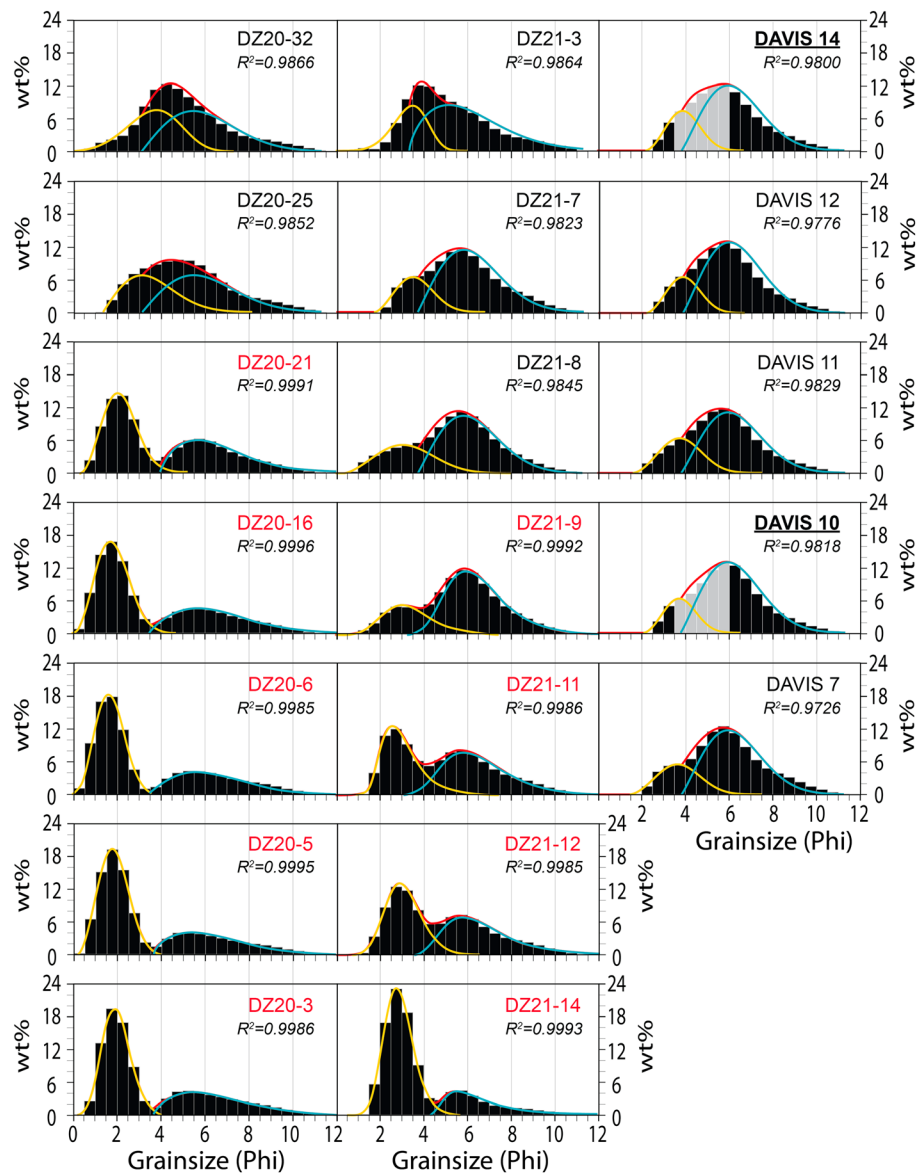


Figure 6. Deconvolved GSDs, with fine subpopulation in blue, coarse in yellow, and simulated bulk distribution in red. The bimodal GSDs are named in red and were deconvolved using DECOLOG 5.0. The other samples were deconvolved by fixing the shape of the fine subpopulation. R^2 (coefficient of determination) measures the fit quality produced by deconvolution. Samples analyzed for componentry are underlined, and approximate grain size range represented by grey histogram bars.

unimodal GSDs present along more northerly and more distal transects; of these, 10 could be deconvolved (located in transects I, II, and III) using the methodology described in section 3.1, and 14 could not (DAVIS1, DAVIS17, DAVIS 21 located in transect III, and all the WOOD and BATE samples located in transects IV and V), because of an overlap between the two subpopulations of more than 70%. We use these data to examine downwind variations in grain size and component characteristics.

4.1. Variations of Grain Size Subpopulations Within Bimodal Samples

The cumulative and probability density functions of $CS_{b,s}$ and $FS_{b,s}$ are presented in Figures 4 and 6, respectively. All deconvolved $FS_{b,s}$ have similar shapes and constant mean values of $\sim 15 \mu m$, but the $CS_{b,s}$ vary strongly both along and across the deposit axis. $CS_{b,s}$ along transect I are substantially coarser than along transect II (mean values plotted in Figures 7b and 7e), as expected for increasing distance from the vent. More

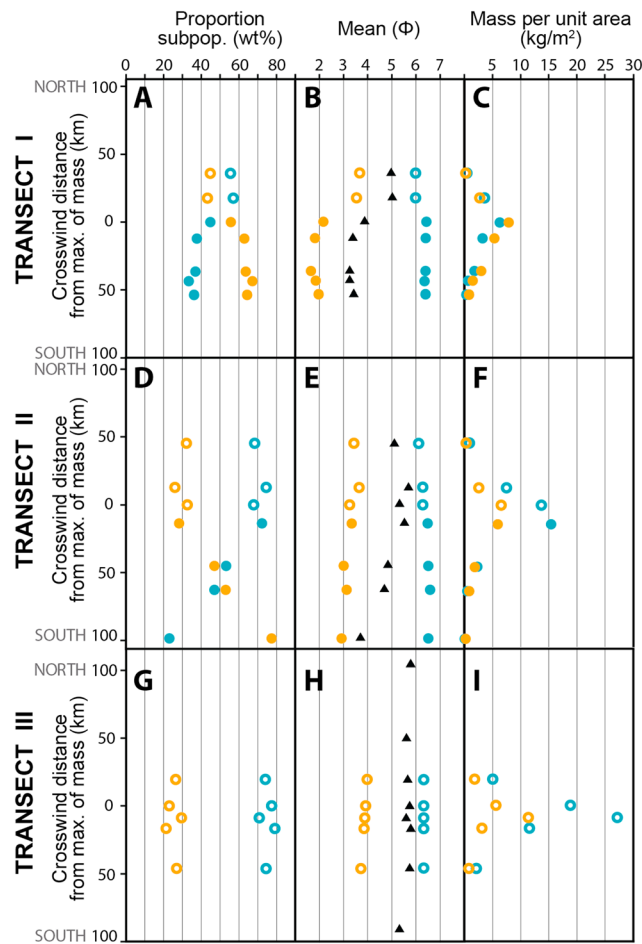


Figure 7. (a–i) Proportion (wt %), mean (Φ), and mass per unit area (kg/m^2) of the coarse (in orange) and fine (in blue) grain size subpopulations obtained by deconvolution in transects I, II, and III. Solid circles represent bimodal samples deconvolved using the fully automated DECOLOG 5.0, open circles represent unimodal samples deconvolved by fixing the fine subpopulation. Black triangles represent bulk distributions (before deconvolution).

generally show poor fits to the fine tail ($\leq 3 \mu\text{m}$; Figure 6). The resulting CS_u distributions complete the trend defined by variations in CS_b s. Along transect I, the two deconvolved unimodal samples are located to the north of the deposit axis, where the CS_u and FS_u proportions are similar to those measured in the northernmost bimodal sample and define a roughly constant trend from the axis to the northern edge of the deposit (Figure 7a). Importantly, however, the CS_u distributions have smaller mean sizes than those of the CS_b s (Figure 7b). The mass per unit area of both subpopulations reaches a maximum on the deposit axis, with both CS_u and FS_u mass decreasing toward the north (Figure 7c).

The three CS_u measurements in transect II are also located within the northern half of the deposit, and their proportion and mass per unit area are similar to those of transect I. Key characteristics include roughly constant CS and FS proportions to the north of the deposit axis (Figure 7d), and mass peaks on, and ~ 20 km south of, the deposit axis for the coarse and fine subpopulations, respectively (Figure 7f). Again, the mean of the CS_u lies within the range of the CS_b mean values from transect I (Figure 7e). In contrast, along transect III both the proportion and mean of the CS_u are constant (Figures 7g and 7h). They are, respectively, lower (20 to 30 wt %) and smaller (mean value around $63 \mu\text{m}$) than in transects I and II. Instead, the fine subpopulations account for much of the mass (Figure 7g), which reaches a maximum on the deposit axis for both CS_b s and FS_b s, consistent with the overall observation of a secondary thickness along this transect (Figure 7i).

unusual is the variation of the mean grain size of the CS_b s along the individual transects. Along transect I, the CS_b mean is largest at 35–40 km south of the deposit axis and decreases in both directions away from this location (Figure 7b). Along transect II, the CS_b mean is coarsest in the southernmost sample collected (100 km south of the deposit axis) and becomes slightly finer toward the north (Figure 7e).

Modal proportions of different grain size fractions also vary both along and across the transport direction. CS_b s prevail over FS_b s along transect I (60–70 versus 30–40 wt %, respectively; Figure 7a), with a slight decrease in the CS_b proportion toward the north. The northernmost bimodal sample (DZ20–21) lies on the deposit axis and comprises 45 wt % coarse and 55 wt % fine subpopulations. In transect II, CS_b is preponderant within the most southern sample, and its proportion decreases abruptly toward the north (Figure 7d). About 50 km south of the deposit axis along this transect, FS_b becomes the dominant grain size fraction.

4.2. Variations of the Grain Size Subpopulations Within the Unimodal Samples

We successfully ($R^2 \geq 0.97$) deconvolved 10 unimodal samples in transects I, II, and III, although these samples gener-

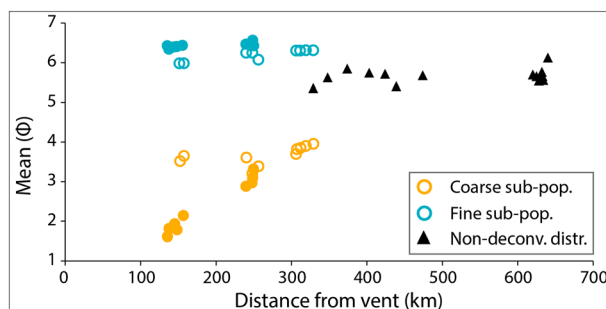


Figure 8. Variation of mean (Φ) versus absolute distance from vent (km) for coarse and fine grain size subpopulations, and for nondeconvolved GSDs. Here solid circles represent the bimodal samples.

4.3. Downwind Changes in GSD Means

Figure 8 shows variations in the mean of the GSDs from all 33 fallout samples, as a function of the absolute distance from the vent. Where deconvolved, CS and FS means are plotted separately (bimodal data as filled circles and unimodal data as open circles). First and foremost, the data show that while the mean of the coarse subpopulation decreases systematically with distance from vent, the mean of the fine subpopulation (FS_b) remains constant at $\sim 6\Phi$ ($16\mu\text{m}$). Two samples that depart from

the CS trend are DZ20-25 and DZ20-32, which are located on the northern part of transect I. The nondeconvolved distributions have mean values close to those of the fine subpopulations and occur at a distance at which the mean variation trends of the coarse and fine subpopulations converge.

4.4. Distribution of the Ash Components

Changes in the proportions of ash components (in both number % and mass %) across the secondary maximum (transect III) and in one of the most distal samples (transect V) are shown in Figure 5e. Along transect III, the abundance of vesicular microlite-poor particles decreases significantly toward the north (from ~ 30 to <5 wt %), while the proportion of accessory (nonjuvenile) particles increases from ~ 16 to ~ 50 wt %. The other components do not show a clear spatial trend. The distal sample from transect V (BATE 12, collected at > 600 km) shows a similar componentry distribution to sample DAVIS 10 (near the secondary thickness maximum in transect III). It contains ~ 9 wt % of microlite-rich particles (componentry class 4; Figure 5) and 41 wt % of microlite-poor juvenile particles (componentry classes 1 and 2). When corrected for mass the samples located within the zone of secondary thickening (DAVIS10 and DAVIS14) contain the same *absolute* amount of dense microlite-poor glass, while the absolute amount of vesicular microlite-poor particles decreases from the southern (DAVIS10) toward the northern sample (DAVIS14) (Table 2). Accessory and microlite-rich particles do not vary significantly.

5. Discussion

In the next sections, we address the origin of both the different ash components and the bimodality of the grain size distributions. We then examine the spatial variations of both the componentry and grain size in the context of reanalysis data of atmospheric wind fields and satellite images of the spreading ash cloud. Finally, we discuss different transport and sedimentation mechanisms likely to explain the depositional patterns highlighted by our results.

5.1. Origin and Transport of the Ash Components

The different ash components identified in the fallout deposit (Figure 5) can be related to the different phases of the eruption. The vesicular microlite-poor glass particles (Figure 5c) were produced by rapid magma transfer from depth to the surface (with associated extensive vesiculation), consistent with the dynamics of the Plinian eruptive phase [Blundy and Cashman, 2001; Klug and Cashman, 1994]. The dense glass particles (Figure 5d) must come from the same vesicular magma and represent the bubble-free melt interstices between larger bubbles. That these glass shards are not significantly smaller than the vesicular particles (Figures 5c and 5d) indicates that the magma contained a wide range of bubble sizes, as inferred from textural studies of the Plinian products [Genareau et al., 2013; Klug and Cashman, 1994]. Phenocrysts and phenocryst fragments included in vesicular microlite-poor glass can also be attributed to the Plinian phase of the eruption. The microlite-rich particles, in contrast, are characteristic of the cryptodome material [Cashman and Hoblitt, 2004; Hoblitt and Harmon, 1993; Hoblitt et al., 1981; Muir et al., 2012]. Also characteristic are the variable bubble contents of these samples and the contorted bubble shapes caused by expansion around groundmass microlites (Figure 5b). Both phenocrysts and phenocryst fragments included in microlite-rich

glass can also be attributed to the cryptodome and thus the blast deposit. The early blast also incorporated abundant nonmagmatic material from the collapsed mountain flank, which was observed in proximal blast deposits [Hoblitt and Harmon, 1993; Hoblitt et al., 1981]. The generally altered nature of the accidental particles observed in the samples studied here (Figure 5a and Data Sets S1 to S6 in the supporting information) suggests material originating from the vicinity of the vent (either 1980 or earlier) or shallow subsurface, and erupted early, most probably during the blast phase. Phenocrysts with no observable adhering glass cannot be definitively identified as blast or Plinian, because phenocryst compositions in the juvenile material from these two eruption phases overlap [Berlo et al., 2007; Hoblitt and Harmon, 1993; Rutherford et al., 1985]. The blast-derived particles (cryptodome fragments, phenocrysts included in cryptodome-like matrix, and accidentals) were necessarily transported in the early co-blast plume (i.e., the co-PDC plume that uplifted from the surge produced by the blast in the early morning). The particles produced during the Plinian phase (dense and vesicular microlite-poor glassy particles, and phenocrysts in a microlite-poor matrix) could have been transported in the vent-derived plumes or in the co-PDC plumes generated by the afternoon pumice flows (hereafter referred to as co-pumice flow plumes) [Carey et al., 1990; Criswell, 1987]. We further hypothesize that vesicular microlite-poor particles with sharp edges, thin walls, and delicate shapes (cf. Data Sets S1 to S6 in the supporting information) are unlikely to be preserved in a PDC where collisional and frictional processes cause abrasion and comminution of the flow material [Calder et al., 2000; Dufek and Manga, 2008; Manga et al., 2011]. We thus infer that the vesicular microlite-poor particles were sourced from vertical activity at the vent, most likely during the late afternoon Plinian phase (Figure 1).

5.2. Origin of the Grain Size Subpopulations

The observed downwind decrease in the mean grain size of the coarse subpopulation (Figures 7b, 7e, 7h, and 8a) is consistent with fractionation during dispersion of a laterally spreading volcanic plume containing a wide GSD (i.e., vent-derived plume), due to sedimentation governed by gravitational settling of individual particles in a turbulent to intermediate regime [Bonadonna et al., 1998; Bursik et al., 1992; Sparks et al., 1992]. The crosswind variations of the mean further suggest that the dispersal axis of the coarse material was displaced to the south of the (mass defined) deposit axis (to ~30, 100, and 50 km south of transects I, II, and III depositional axes, respectively). The coarse subpopulations obtained from deconvolving the unimodal samples (by fixing the fine subpopulation) complete the trend observed in the bimodal samples, consistent with decreasing size of the coarse population and an assumed constant fine subpopulation at 12–16 μm , or 6 to 6.4 Φ (Figures 4 and 8a). From this perspective, the distributions that we were not able to deconvolve (DAVIS1, DAVIS17, DAVIS 21, and all the WOOD and BATE samples; Figure 3) might also be a mixture of a constant fine and a slightly coarser subpopulation, which lies within the limiting 70% overlap in grain size that prevented deconvolution.

Similar patterns of bimodal grain size distributions have been observed in fallout deposits from eruptions with sizes that range from intermediate (e.g., the 1997 Vulcanian explosions of Soufriere Hills, Montserrat, Bonadonna et al. [2002] and the August 2006 Tungurahua Subplinian eruption, Eychenne et al. [2012]) to large (the June 1991 Pinatubo Plinian eruption, Wiesner et al. [2004]) to very large and ignimbrite-forming eruptions (e.g., the Campanian eruption from the Phlegraean Fields, Engwell et al. [2014b] and Sparks and Huang [1980], and the Minoan eruption of Santorini, Sparks et al. [1984] and Sparks and Huang [1980]). Fallout deposits from the latter two eruptions appear as coarse lower and fine upper units in proximal locations, as a massive ash layer with bimodal GSDs in medial locations, and as a massive unimodal ash layer in distal locations. In these examples, the mean grain size of the distal unimodal samples is identical to the fine peak of the medial bimodal ash layers [Engwell et al., 2014b; Sparks and Huang, 1980]. Here the coarse subpopulation is inferred to derive from a Plinian eruptive plume formed at the vent, while the fine subpopulation is interpreted as ash settling from co-PDC plumes forming during emplacement of the (subsequent) ignimbrite flows [Engwell et al., 2014a; Engwell et al., 2014b; Sparks et al., 1984; Sparks and Huang, 1980]. This interpretation is supported by both the fine-grained nature of the ash layer and its relative enrichment in glassy material, which are characteristics of co-ignimbrite deposits observed on land [Sparks and Walker, 1977]. The spatial pattern of 1991 Pinatubo fallout ash sampled in South China deep sea cores has been interpreted the same way [Wiesner et al., 2004]. Similarly, bimodal GSDs in the Tungurahua fallout deposit have been interpreted as mixed fallout and co-PDC ash, as demonstrated by correlating the enrichment trend in the deposit (determined from the proportion of the fine peak) to the zone of main PDC emplacement on the volcano's flank [Eychenne et al., 2012]. At Montserrat, syn-eruptive PDC activity observed during the 1997 series of Vulcanian explosions has also been correlated with the occurrence of bimodal grain size distributions in the fallout deposit

[Bonadonna *et al.*, 2002]. Critically, all examples show a constant fine grain size mode at $\sim 5\text{--}6 \Phi$ regardless of the distance from vent; this characteristic may reflect the physical processes controlling the entrainment of particles from PDCs to co-PDC plumes and/or the mechanisms governing their dispersion and sedimentation (see discussion below). The characteristics of the fine subpopulation retrieved from the bimodal samples of the Mount St. Helens fallout deposit are thus consistent with a co-PDC origin (either from the co-blast or co-pumice flow plumes).

5.3. A Composite Fallout Deposit From Multiple Sources of Ash

Both the grain size and componentry data indicate that at distances greater than 150 km from vent, the Mount St. Helens fallout deposit is composite, with material originating from both vent-derived (Plinian phase) and co-PDC (co-blast or co-pumice flow) plumes. The relative proportions of coarse and fine subpopulations, along with the crosswind variations of the coarse subpopulation mean, indicate that vent-derived particles are enriched to the south of the deposit axis, particularly in transects I and II (Figures 7a–7h). The componentry distributions in transect III also show both a relative and an absolute increase in Plinian phase particles toward the south, with a progressive increase in blast-derived particles toward the north (Figure 5e and Table 2). Interestingly, componentry of distal sample BATE 12 shows that the distribution of components does not vary significantly along the deposit axis between 300 and >600 km from the vent, suggesting that blast- and Plinian-derived particles reached the same distance downwind but were heterogeneously distributed across the plume dispersion axis.

Componentry alone cannot be used to distinguish particles transported in co-pumice flow plumes produced by the afternoon eruptive activity [Carey *et al.*, 1990; Criswell, 1987] (Figure 1) from tephra produced by the vent-derived Plinian column. However, given the poor preservation potential of vesicular material containing thin bubble walls within a PDC [Dufek and Manga, 2008], co-pumice flow particles are likely to contribute primarily to the dense microlite-free glass, which does not show a crosswind trend. The correlation between the measured proportions of the fine subpopulation (FS) and the trends in componentry thus suggests that the co-PDC signature identifiable in the FS derives primarily from co-blast ash, although co-pumice flow ash might also contribute a modest amount. Overall, these findings demonstrate that the co-blast plume was an exceptionally efficient mechanism of fine ash formation and injection into the atmosphere and produced a fallout deposit with an unusually large amount of fine ash compared to other Subplinian and Plinian eruptions [e.g., Rust and Cashman, 2011].

5.4. Dispersion Processes

The multiple sources of ash only partially explain the heterogeneity of the fallout deposit; additional explanations can be found in complex and changing dispersion processes with time. Here we constrain these processes by revisiting original observations of plume transport and reanalyzed wind data.

5.4.1. Published Observations of Plume Dispersion

GOES visible images (at 8:50 and 9:20 PDT) show that less than 20 min after the eruption started, the circular umbrella cloud was ~ 80 km in diameter and centered north of the mountain [Holasek and Self, 1995; Pouget *et al.*, 2013]. It corresponds to the early co-blast plume, which uplifted from the entire area covered by the surge (≤ 15 km north of the vent) [Sparks *et al.*, 1986]. According to classified satellite images [Sparks *et al.*, 1986], the giant umbrella cloud reached a maximum height of >30 km in about 20 min, consistent with the maximum heights estimated from the GOES images at 8:50 and 9:20 PDT [Holasek and Self, 1995] (Figure 1). At 9:20, the top of the plume was still at 30 km and the umbrella region extended more than 100 km toward the north but *did not progress toward the south*; this asymmetry was a consequence of the strong northward momentum of the co-blast plume created by the high directional energy of the blast [Druitt, 1992; Esposti Ongaro *et al.*, 2011; Hoblitt, 2000; Kieffer, 1981]. The strong northward momentum of the plume is confirmed by photographs of the co-blast plume taken from the ground at 8:50, which show a very wide plume that increases rapidly in diameter with height and is bent to the north [Sparks *et al.*, 1986]. Critically, we suggest that this northward momentum explains the observed north-south asymmetry of the deposit isomass and isopach lines close to the vent [Carey and Sigurdsson, 1982; Sarna-Wojcicki *et al.*, 1981] (Figure 2). Momentum-driven northward displacement of the plume may also explain the reported difficulties in replicating aspects of ash transport and deposition with advection-diffusion models, and the necessity of displacing the source tens of kilometers north of the actual source of the co-blast plume [Armienti *et al.*, 1988; Folch *et al.*, 2010].

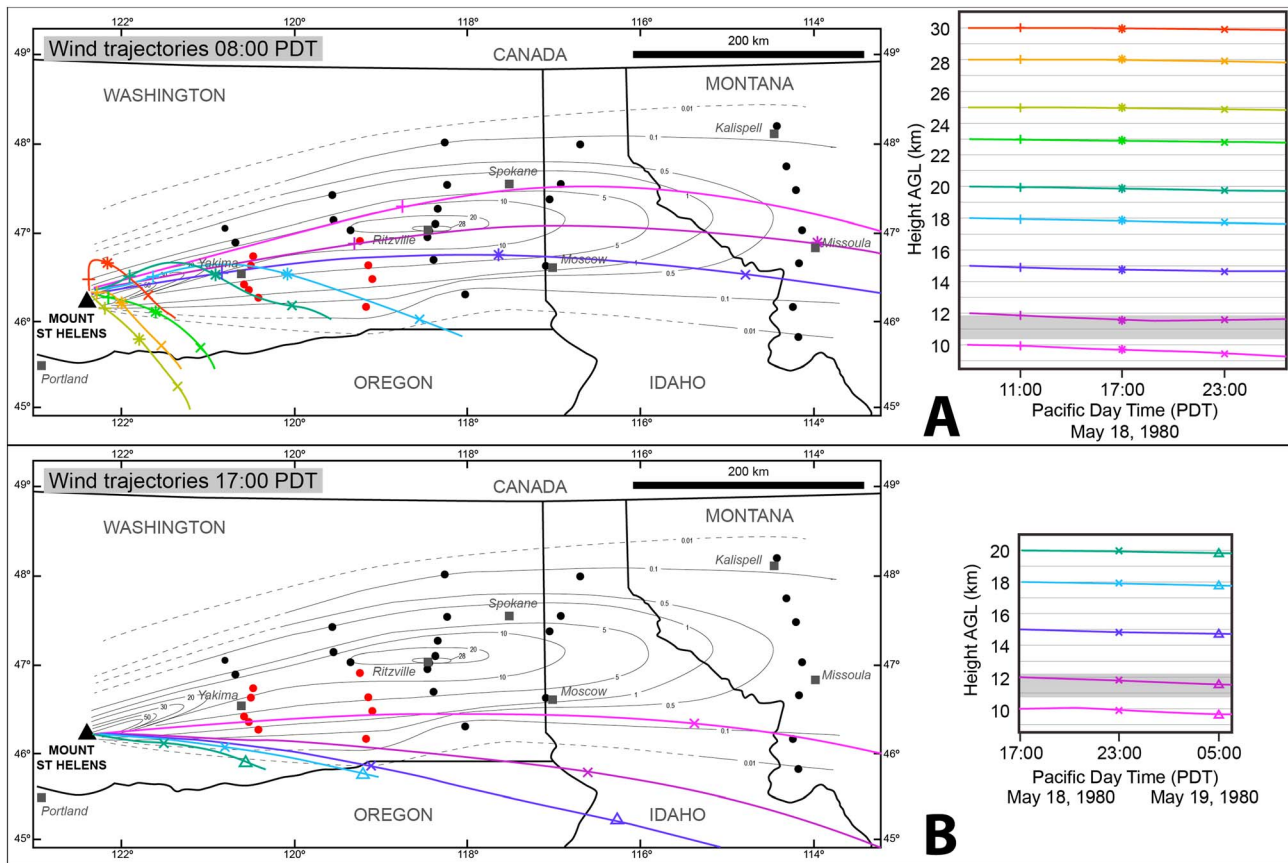


Figure 9. Air parcel trajectories (analogous to wind trajectories) at different pressure levels for a source above Mount St. Helens volcano at (a) 8.00 and (b) 17.00 PDT on 18 May 1980, calculated using the HYSPLIT model (NOAA Air Resources Laboratory) and reanalysis meteorological data (National Centers for Environmental Prediction/National Center for Atmospheric Research Global Reanalysis Data Archive). Right-hand diagrams represent corresponding heights (above ground level) with time of each pressure-based trajectory plotted on maps. Each symbol type drawn along mapped trajectories represents a similar time and date (see right-hand diagrams). The grey shaded areas on the right-hand diagrams represent the approximate height of the tropopause [Holasek and Self, 1995].

Satellite images show that by 9:20, ash was spreading to the east and southeast at much lower altitudes than the 30 km plume top (see Plate 1a of Holasek and Self [1995]). By 9:50, this low-altitude plume was strongly elongated to the east; at the same time, the top of the plume (with a diameter of ~100 km) had detached from the vent and slowly progressed to the north. From 9:20 until at least 11:20, no plume is visible above the vent on the GOES images (Figure 1), which might be a consequence of the large shadow cast by the high co-blast plume. Indeed, ground observers reported that a moderately high vertical column was emitted from the vent after 9:00 [Criswell, 1987]. The maximum plume heights of 30 km measured by Holasek and Self [1995] during this time interval must thus represent the top of the co-blast plume, which subsided throughout the morning to an altitude of about 15 km. The vent-derived plume top was lower and is probably what was measured by the meteorological radar located in Portland, Oregon (~80 km south-south east of the volcano), which reports a 14 km high plume during this time interval [Harris et al., 1981]. This plume would also have dispersed toward the east.

5.4.2. Wind and Ash Dispersal Directions

The wind speed and direction at the time of the eruption have been determined at different atmospheric levels using the trajectory model Hybrid Single-Particle Lagrangian Integrated Trajectory (HYSPLIT), based on reanalysis meteorological data (Figure 9). These data indicate that from 8:00 to 11:00 PDT, the wind was blowing toward the east at elevations of 10–20 km, with maximum velocities > 100 km/h located near the tropopause (10–12 km). At higher elevations, the wind direction was toward the south-east at very low velocities; at the maximum altitude of the co-blast plume (30 km), there was almost no wind (Figure 9a). Between 11:00 and 17:00, the atmospheric winds maintained an eastward direction and high velocities at altitudes of 10–15 km; the winds were dominantly southeasterly at elevations ≥ 18 km (Figure 9a). After 17:00, the winds shifted to an east-south-east direction at elevations between 10 and 20 km, with a high-velocity layer still located between 10 and 12 km (Figure 9b).

The speed of the high-velocity layer between 8:00 and 11:00 PDT is consistent with the average speed at which the plume dispersed to the east, as constrained by the satellite images (Figure 1 and Table S2 in the supporting information). These images show that both the co-blast and early-vent-derived material spread eastward in this high-velocity layer at an altitude of ~10–12 km (Figure 9a). The significant difference between the co-blast plume top height (30 km) and the height at which the material was preferentially dispersed (10–12 km) testifies to momentum-driven overshoot of the co-blast plume above the level of neutral buoyancy [Sparks *et al.*, 1986] and to the control of wind conditions on the lateral injection height of ash into the atmosphere. Critically, the absence of wind toward the top of the co-blast plume limited dispersal at this altitude; for this reason, ash was dispersed eastward only after it settled into the high-velocity layer near the tropopause. These complex proximal dispersion processes may explain why published advection-diffusion-sedimentation models have failed to reproduce the proximal area of the Mount St. Helens fallout deposit [Armienti *et al.*, 1988; Fero *et al.*, 2008] and have produced an optimal fit of the medial to distal deposit trend by displacing the emission source well to the north of the vent [e.g., Folch *et al.*, 2010].

Wind conditions between 11:00 and 17:00 (Figures 1 and 9a) indicate that plumes (both vertical and co-pumice flows) produced during the afternoon eruptive activity also dispersed toward the east in the high-velocity atmospheric layer at 10–12 km height. Co-pumice flow ash was thus distributed over approximately the same area as the co-blast ash, except that the co-pumice flow ash did not travel as far to the north because it lacked the northward lateral momentum. The shift in direction of the high-velocity layer to the ESE after 17:00 (Figure 9b) suggests that ash erupted during the late Plinian phase, which produced a plume of ≤ 20 km height, must have dispersed in a more southerly direction. This is consistent with both grain size and componentry data (Figures 5 and 7), which show that coarse mode of the Plinian ash was dispersed to the south of the main deposit axis.

5.5. Sedimentation Processes

5.5.1. Sedimentation Behaviors of the Grain Size Subpopulations

The contrasting grain size patterns of ash deposits from vent-derived (Plinian) and co-PDC plumes reveal important differences in sedimentation processes. In proximal and medial areas, settling from vent-derived plumes, which, at these distances, are dominated by particles that are heterogeneous in size and coarser than about $> 125 \mu\text{m}$, can be explained by changes in individual particle settling velocities as grain size decreases with distance from vent [Bonadonna *et al.*, 1998; Rose, 1993]. Co-PDC plumes, in contrast, contain mostly fine material, irrespective of the type of PDCs they derive from, and deposit fine-grained material even close to source (e.g., 70% of co-ignimbrite particles $< 125 \mu\text{m}$) [Sparks *et al.*, 1973; Sparks and Walker, 1977]. The widespread nature of co-PDC deposits, along with the constancy of their grain size with distance from source (e.g., Figure 8), indicates that sedimentation cannot be controlled by individual settling processes of low Reynolds number particles [Bonadonna *et al.*, 1998]. Some other mechanisms must therefore govern the sedimentation of fine ash at the distances considered here. Distal (nondeconvolved) unimodal distributions also depict a constant mean grain size with distance from source, while componentry of sample BATE 12 (Figure 5) suggests that these samples still contain ash of mixed origin (i.e., co-blast and Plinian plumes). These unimodal distributions occur at a distance (both downwind and crosswind) where the vent-derived plume, depleted in coarser material, contains only particles of similar size to the co-blast plume (Figure 8). Consequently, the constant GSD with distance [see also Durant *et al.*, 2009] results from the specific sedimentation mechanisms governing the settling of particles finer than a threshold size (around $63 \mu\text{m}$), irrespective of the type of plume (vent derived or co-PDC).

Profiles of mass per unit area (Figures 7e, 7f, and 7i) show that the sedimentation maxima of both the co-blast and vent-derived plumes (integrated throughout the whole eruption) are superimposed on the ground, despite some variations in their primary dispersal direction. Importantly, however, while the ash transported in the co-blast plume was injected into the atmosphere over a short time period (tens of minutes), vent-derived material was emitted at a variable discharge rate over the entire day (Figure 1) [Carey *et al.*, 1990; Criswell, 1987]. We suggest that the small grain size of the co-blast ash particles and the absence of wind at the top of the plume (Figure 9a) allowed them to remain suspended for a long time, and, for this reason, that co-blast and vent-derived ash were most likely mixed *during transport*. Additionally, the superposition of the mass per unit area profiles (Figures 7c, 7f and 7i) suggests that *sedimentation was enhanced where the two plumes overlapped*.

Additional information is provided by the recorded times of first ash fall (Figures 1 and 2), which show that, consistent with the small size of the co-blast ash (Figure 3), sedimentation was delayed toward the north relative to

the south. From these data, we conclude that early sedimentation of mixed bimodal ash in the south relative to the fine ash in the north could be related to the interaction of particles, whereby the large particles aided the sedimentation of the small particles (discussed below). In fact, time series samples collected about 200 km downwind (locations WD and H in Figure 2) show that the size distribution of ash falling during the periods of high accumulation rates was bimodal, and that more fine material was deposited near the dispersal axis than toward the southern edge of the deposit [Scheidegger *et al.*, 1982]. Although Scheidegger *et al.* [1982] make no mention of obvious ash aggregates or ash clusters falling at their sampling locations in the medial area (locations WD, PRD, and H in Figure 2) at any time during collection (from ~11:30 to 06:00 the next day), ash clusters were reported to fall (1) at Pullman, Washington, almost 400 km from the vent (Figure 2), where GSDs are not bimodal (Figure 3) and where the mean grain size has stabilized at $\sim 5.5 \phi$ ($22 \mu\text{m}$, Figure 8) [Sorem, 1982], and (2) at Kennewick, Washington, located on the south edge of the fallout deposit, ~ 10 km south of sample DZ21-14 and ~ 230 km from the vent [Rose *et al.*, 1982]. It is important to note that these observations are among the first to have been made of falling ash aggregates, and that lack of aggregate observations in the medial area cannot strictly be interpreted as absence of falling aggregates.

Finally, mass per unit area profiles (Figures 7a, 7f, and 7i) show that the absolute amount of ash in the coarse (mostly vent-derived) subpopulation remains approximately constant downwind, even though the mean grain size decreases substantially (Figure 8). In contrast, the absolute amount of ash in the uniformly fine (mostly co-blast) subpopulation increases sharply toward the area of maximum secondary thickening at about 300 km from vent (transect III, Figure 7i). This observation suggests enhanced sedimentation of fine ash in this region (i.e., increased sedimentation rate), as suggested by previous workers [Carey and Sigurdsson, 1982; Durant *et al.*, 2009].

5.5.2. Mechanisms for Enhanced Sedimentation

The process of enhanced sedimentation most commonly invoked to explain polymodal GSDs in distal fallout deposits, and secondary thickness maxima is aggregation of fine particles to form coarser pellets or clusters; these aggregates are then deposited "prematurely" due to their higher terminal velocity [e.g., Carey and Sigurdsson, 1982; Schumacher, 1994]. More recent analysis further suggests that aggregate type changes from proximal to distal locations and aggregation is a temporally dynamic process [Brown *et al.*, 2012]. In proximal regions, where ash concentration in both vent-derived and co-PDC plumes is high, subspherical accretionary pellets (aggregates of concentric layers of particles sometimes organized around a larger particle) can be abundant [e.g., Bonadonna *et al.*, 2002; Brazier *et al.*, 1982; Brown *et al.*, 2003]. In medial to distal regions (>100 km from source), only irregularly shaped loose ash clusters or particles coated by finer adhering grains have been observed [Bonadonna *et al.*, 2011; Sorem, 1982]. Although wet aggregation is a dominant process, the role of electrostatic forces [Gilbert and Lane, 1994], ice nucleation, and precipitation of secondary phases on particle surfaces is also significant, particularly in distal, weakly concentrated ash clouds [Brown *et al.*, 2012; Gislason *et al.*, 2011; Van Eaton *et al.*, 2012].

Apart from the accretionary pellets recorded in the proximal blast deposits [e.g., Criswell, 1987; Druitt, 1992; Hoblitt *et al.*, 1981], evidence of sedimentation of ash clusters in the medial and distal Mount St. Helens fallout deposit is rare (examples are listed in section 5.5.1). An experimental study of electrostatic ash clustering performed on natural ash $< 250 \mu\text{m}$ in size [Schumacher, 1994] roughly reproduced the downwind, along axis, grain size variations in the 18 May 1980 Mount St. Helens fallout deposit. This study reproduces grain size distributions with a mode at $90 \mu\text{m}$ when single particles are coated with finer particles, while fine ash clustering produces wide distributions with a mode between 45 and $15 \mu\text{m}$. Schumacher [1994] concluded that particle coating dominated in the proximal regions, while ash clustering was the primary aggregation style in distal regions, and that both processes were of similar importance in the medial area, thus generating bimodal GSDs. This work does not explain the crosswind variations of grain size, however, and more importantly does not account for the prominent area of secondary thickness and mass observed in the isopach and isomass maps.

Numerical models of ash sedimentation that include an aggregation scheme were first constructed using empirical parameterizations [Armienti *et al.*, 1988; Carey and Sigurdsson, 1982; Cornell *et al.*, 1983], whereby particles smaller than a threshold size were assumed to form clusters of a given size and density or to settle at a fixed terminal velocity. The early models applied to Mount St. Helens considered that all particles $< 63 \mu\text{m}$ aggregated [Armienti *et al.*, 1988; Carey and Sigurdsson, 1982]. While simulations of Carey and Sigurdsson [1982] reproduced the secondary maximum along the axis, they could not explain the proximal fine ash deposition. Armienti *et al.* [1988] also match the along-axis location of the secondary maximum, but it lies 10–20 km south of the actual deposit, even though they moved the volcanic source 40 km north

of the actual vent. A more complex model of wet aggregation was developed by *Costa et al.* [2010], who used a fractal law to describe the aggregation rate. Application of this model to Mount St. Helens also reproduces an area of secondary thickness [*Folch et al.*, 2010], but the simulated deposits are much narrower than the observed deposit, are systematically displaced to the south, and the area of secondary maximum extends ~60 km closer to source than observed.

The presence of a secondary thickness and mass maximum at > 250 km from source implies a relatively abrupt change of sedimentation conditions. There is no obvious reason why aggregation rates would increase abruptly in this region given the absence of rain. Alternative models for enhanced sedimentation involve the bulk dynamics of the dispersing cloud rather than the behavior of individual or clustered particles. They also account for the observation of pronounced mammatus at the base of the dispersing cloud above the medial area of the deposit [*Durant et al.*, 2009; *Schultz et al.*, 2006; *Waite*, 2015]. *Durant et al.* [2009] proposed a conceptual model for the formation of mammatus in volcanic clouds: ash particles in the cloud act as ice nuclei and ice hydrometeors form on ash particles, increasing mass and settling velocity. In this model, the high water vapor content of the Mount St. Helens cloud (derived from magmatic volatiles and entrainment of moist lower tropospheric air) drove abundant ice crystal growth. These hydrometeors accumulated at the cloud base and sublimated on contact with the ambient atmosphere, causing subsidence from the associated latent heat combined with gravitational loading. Moderately turbulent mammatus lobes form at some critical threshold of ice particle number concentration and size [*Schultz et al.*, 2006]. As the cloud layer passed through the melting level at about 6.9 km altitude, the rate of aggregation increased rapidly in response to the sudden availability of liquid water, and a surge of loosely bound fine ash reached the ground, producing the distal mass accumulation maximum in the deposit.

Another model to explain the mammatus-like base of the cloud was proposed by *Carazzo and Jellinek* [2012, 2013] and relates to the development of “particle boundary layers” (PBLs) that retain small particles at the base of spreading plumes by a mechanism of diffusive convection. The development of PBLs is favored by interaction of particles of different sizes and a high content of fine ash [*Carazzo and Jellinek*, 2013]. These PBLs can also periodically detach from the cloud and settle en-masse due to gravitational instabilities [*Carazzo and Jellinek*, 2012]. For example, gravitational instabilities observed close to the vent during the 2010 Eyjafjallajökull eruption (Iceland) channeled small and large particles to the ground at similar speeds [*Manzella et al.*, 2015]. Additionally, when the time of first ash fall from the Mount St. Helens plume displayed in Figure 2 [after *Quinn*, 1982] is compared with a numerical sedimentation model that did not include aggregation, not one but two cycles of delayed and accelerated ash fall with periods of 300 km can be seen [*Hopkins and Bridgman*, 1985, Figure 4]. This cyclicity is consistent with a model of periodic en-masse release of particles. From this, we suggest that the small absolute increase in the mass of the coarse subpopulation (which here has a mean size of 63 μm) in transect III, the significant increase in the fine subpopulation (with a mean size ~15 μm ; Figure 7i), and the asymmetry of individual GSDs across the region of secondary thickening (250 to 350 km from vent; Figure 2) could all be explained by en-masse fallout from PBLs that were enhanced by the high fine ash content of the Mount St. Helens cloud. Additional aggregation and formation of hydrometeors within the boundary layers, as suggested by *Durant et al.* [2009], would have added to the fine ash fallout in the region of the secondary mass maximum.

Finally, as stated above, the observed crosswind variations of mass per unit area (Figure 7) are at odds with simple aggregation processes and instead indicate enhanced sedimentation of small particles where coarser vent-derived material interacted with small (co-blast) particles during transport. Coating of coarser particles by fine ash is one possible mechanism, another is entrainment of small particles during (faster) sedimentation of larger particles. Particle coating could lead to higher absolute rates of sedimentation as the size difference between small and large particles decreases, because of an increase of the surface area available for coating. This hypothesis provides an additional mechanism by which mass deposition may be enhanced in the area of secondary mass maximum, where grain size subpopulations start to overlap (Figures 3 and 6).

5.5.3. Reappraisal of the Mass Eruptive Budget

Finally, the results of this study allow us to reassess the mass budget of the eruption. *Sarna-Wojcicki et al.* [1981] used planimetry to estimate the total mass of the fallout deposit from the isomass map shown in Figure 2 at $4.9\text{--}5.5 \times 10^{11}$ kg. We use our data to assess the contribution of different populations of ash grains (coarse and fine; blast and Plinian) in the analyzed region (between transects I and III, i.e., ~150 to ~320 km

from vent). By integrating both the mass per unit area across the plume axis (Figures 7c, 7f, and 7i) and the mass per unit length along the dispersal axis, we calculate a total mass of 1.2×10^{11} kg for this part of the deposit (~20% of the total deposit calculated by *Sarna-Wojcicki et al.* [1981]). Of this, the mass is approximately equally divided between the coarse and fine subpopulations (5.8 and 6.2×10^{10} kg, respectively). Considering that most of the fine subpopulation is likely to have a co-blast origin, these results indicate that co-blast ash accounts for at least 50% of the medial fallout deposit. The high contribution of co-blast material in the fallout deposit is also confirmed by componentry analyses performed by *Scheidegger et al.* [1982] on the time series samples collected at Wanapum Dam (WD, Figure 2), which show that microlite-rich particles dominated samples that account for 97% of the total mass (that is ash collected between 11:30 and 19:30 PDT). The large contribution of co-blast ash to the total deposit also explains the difficulties encountered in numerical models of ash dispersion and deposition [*Armenti et al.*, 1988; *Folch et al.*, 2010], all of which have thus far assumed that much of the distal mass was emitted from a Plinian column that persisted for the entire duration of the eruption.

Finally, the large contribution of co-PDC (and probably largely co-blast) ash explains the extremely small median grain size of the total grain size distribution for this deposit [*Rose and Durant*, 2009; *Rust and Cashman*, 2011]. Additionally, the componentry distributions show that at least 16 wt %, and plausibly as much as 52 wt %, of the ash in this part of the deposit is not juvenile (Figure 5e). If this is representative of the componentry of the deposit as a whole, then the magma volume erupted on 18 May may have been overestimated by up to a factor of 2.

6. Conclusion

The complex depositional pattern of the fallout deposit from the 18 May 1980 Mount St. Helens eruption results from the unusual eruptive dynamics, which strongly impacted the dispersion and sedimentation processes. The co-blast plume, in particular, was an exceptionally efficient mechanism for supplying fine ash to the atmosphere and explains the remarkably high fine ash content of the fallout deposit from this eruption. Contributions to the sustained dispersing cloud from the two different main sources (co-blast and vent-derived plumes) created a pronounced crosswind asymmetry to both individual grain size and componentry distributions, which could not have been unraveled without detailed analyses of these parameters in individual tephra samples. Fine ash is present throughout the deposit but settled at an increased rate distally and reached the ground approximately 250–300 km from the volcano producing the area of secondary thickness and mass maximum. The sedimentation of fine ash was most likely controlled by a combination of enhanced settling mechanisms that include, but are not limited to, aggregation. Gravitational convective instabilities of cloud base particle boundary layers, hydrometeor formation, and destruction due to the interaction of the ash cloud with different atmospheric layers, and entrainment of fine particles by larger ones, may also have played important roles. Together, these processes ultimately determined the atmospheric lifetime of the fine ash.

Critical for the proximal sedimentation pattern was the horizontal (northward) momentum that drove the co-blast plume toward the north, eventually causing it to detach from the vent; at the same time, ash was progressively dispersed toward the east in the lower high-velocity winds at altitudes of 10–12 km. The early blast caused an overall displacement of the deposit toward the north as well as the north-south asymmetry of the isomass map, which has not yet been reproduced by advection-diffusion models. At distances beyond ~100 km from the volcano, ash was transported primarily within a high wind velocity layer at 10–12 km altitude, significantly lower than the maximum height of the co-blast plume. This presents a cautionary note about the use of maximum plume height as a measure of the altitude of lateral dispersion of material in the atmosphere, or as a measure of the mass eruption rate. In this case, the high vertical ascent rate was transitory.

Our findings also highlight the importance of considering individual phases of an eruption for the understanding of its dynamics, and the potentially contrasting behavior of co-PDC and vent-derived plumes. In the case of the Mount St. Helens eruption, a critical analysis of the field data is essential to assess the impact of the complex eruption dynamics on the depositional pattern of the fallout. This represents a critical step toward unraveling the combined effects of multiple eruptive processes and plume types on ensemble characteristics of eruptions, such as magmatic budgets, total grain size distributions, and fragmentation mechanisms.

Acknowledgments

J. Eychenne was funded by the People Programme (Intra-European Fellowship) of the European Union's Seventh Framework Programme (FP7). K. Cashman was supported by the AXA Research Fund, and A. Rust by a Royal Society University Research Fellowship. We thank Editor André Revil, as well as Costanza Bonadonna and Larry Mastin for thoughtful and constructive comments that greatly enhanced the quality of the manuscript. Supporting information, such as original SEM images of ash samples, accompanies this paper.

References

- Andrews, B. J., and M. Manga (2012), Experimental study of turbulence, sedimentation, and co-ignimbrite mass partitioning in dilute pyroclastic density currents, *J. Volcanol. Geotherm. Res.*, 225–226, 30–44.
- Armienti, P., G. Macedonio, and M. T. Pareschi (1988), A numerical model for simulation of tephra transport and deposition: Applications to May 18, 1980, Mount St. Helens eruption, *J. Geophys. Res.*, 93(B6), 6463–6476, doi:10.1029/JB093iB06p06463.
- Beckett, F. M., C. S. Witham, M. Hort, J. A. Stevenson, C. Bonadonna, and S. C. Millington (2014), The sensitivity of NAME forecasts of the transport of volcanic ash clouds to the physical characteristics assigned to the particles, UK Met Office Forecasting Res. Tech. Rep., 592.
- Bellotti, F., L. Capra, D. Sarocchi, and M. D'Antonio (2010), Geostatistics and multivariate analysis as a tool to characterize volcanoclastic deposits: Application to Nevado de Toluca volcano, Mexico, *J. Volcanol. Geotherm. Res.*, 191(1–2), 117–128.
- Berlo, K., J. Blundy, S. Turner, and C. Hawkesworth (2007), Textural and chemical variation in plagioclase phenocrysts from the 1980 eruptions of Mount St. Helens, USA, *Contrib. Mineral. Petrol.*, 154(3), 291–308.
- Bingemer, H., et al. (2012), Atmospheric ice nuclei in the Eyjafjallajökull volcanic ash plume, *Atmos. Chem. Phys.*, 12, 857–867.
- Blundy, J., and K. V. Cashman (2001), Ascent-driven crystallisation of dacite magmas at Mount St. Helens, 1980–1986, *Contrib. Mineral. Petrol.*, 140, 631–650.
- Bonadonna, C., and B. F. Houghton (2005), Total grain-size distribution and volume of tephra-fall deposits, *Bull. Volcanol.*, 67(5), 441–456.
- Bonadonna, C., G. G. J. Ernst, and R. S. J. Sparks (1998), Thickness variations and volume estimates of tephra fall deposits: The importance of particle Reynolds number, *J. Volcanol. Geotherm. Res.*, 81(3–4), 173–187.
- Bonadonna, C., et al. (2002), Tephra fallout in the eruption of Soufriere Hills Volcano, Montserrat, *Geol. Soc. London Mem.*, 21(1), 483–516.
- Bonadonna, C., R. Genco, M. Gouhier, M. Pistolesi, R. Cioni, F. Alfano, A. Hoskuldsson, and M. Ripepe (2011), Tephra sedimentation during the 2010 Eyjafjallajökull eruption (Iceland) from deposit, radar, and satellite observations, *J. Geophys. Res.*, 116, B12202, doi:10.1029/2011JB008462.
- Bonadonna, C., R. Cioni, M. Pistolesi, M. Elisondo, and V. Baumann (2015), Sedimentation of long-lasting wind-affected volcanic plumes: The example of the 2011 rhyolitic Cordón Caulle eruption, Chile, *Bull. Volcanol.*, 77(2), 1–19.
- Brazier, S., A. N. Davis, H. Sigurdsson, and R. S. J. Sparks (1982), Fall-out and deposition of volcanic ash during the 1979 explosive eruption of the Soufriere of St. Vincent, *J. Volcanol. Geotherm. Res.*, 14(3–4), 335–359.
- Brown, R. J., T. L. Barry, M. J. Branney, M. S. Pringle, and S. E. Bryan (2003), The Quaternary pyroclastic succession of southeast Tenerife, Canary Islands: Explosive eruptions, related caldera subsidence, and sector collapse, *Geol. Mag.*, 140(03), 265–288.
- Brown, R. J., C. Bonadonna, and A. J. Durant (2012), A review of volcanic ash aggregation, *Phys. Chem. Earth, Parts A/B/C*, 45–46, 65–78.
- Bursik, M. I., R. S. J. Sparks, J. S. Gilbert, and S. N. Carey (1992), Sedimentation of tephra by volcanic plumes: I. Theory and its comparison with a study of the Fogo A Plinian deposit, Sao Miguel (Azores), *Bull. Volcanol.*, 54(4), 329–344.
- Caballero, L., D. Sarocchi, E. Soto, and L. Borselli (2014), Rheological changes induced by clast fragmentation in debris flows, *J. Geophys. Res. Earth Surf.*, 119, 1800–1817, doi:10.1002/2013JF002942.
- Calder, E. S., R. S. J. Sparks, and M. C. Gardeweg (2000), Erosion, transport and segregation of pumice and lithic clasts in pyroclastic flows inferred from ignimbrite at Lascar Volcano, Chile, *J. Volcanol. Geotherm. Res.*, 104(1–4), 201–235.
- Carazzo, G., and A. M. Jellinek (2012), A new view of the dynamics, stability and longevity of volcanic clouds, *Earth Planet. Sci. Lett.*, 325–326, 39–51.
- Carazzo, G., and A. M. Jellinek (2013), Particle sedimentation and diffusive convection in volcanic ash-clouds, *J. Geophys. Res. Solid Earth*, 118, 1420–1437, doi:10.1002/jgrb.50155.
- Carey, S., and R. S. J. Sparks (1986), Quantitative models of the fallout and dispersal of tephra from volcanic eruption columns, *Bull. Volcanol.*, 48(2), 109–125.
- Carey, S., H. Sigurdsson, J. E. Gardner, and C. W. Criswell (1990), Variations in column height and magma discharge during the May 18, 1980 eruption of Mount St Helens, *J. Volcanol. Geotherm. Res.*, 43, 99–112.
- Carey, S. N., and H. Sigurdsson (1982), Influence of particle aggregation on deposition of distal tephra from the May 18, 1980, eruption of Mount St. Helens volcano, *J. Geophys. Res.*, 87(B8), 7061–7072, doi:10.1029/JB087iB08p07061.
- Casadevall, T., P. Delos Reyes, and D. Schneider (1996), The 1991 Pinatubo eruptions and their effects on aircraft operations, in *Fire and Mud: Eruptions and Lahars of Mount Pinatubo*, edited by C. G. Newhall and R. S. Punongbayan, pp. 625–636, Phil. Inst. Volcanol. and Seismolog., Quezon City, Philippines.
- Cashman, K. V., and R. P. Hoblitt (2004), Magmatic precursors to the 18 May 1980 eruption of Mount St. Helens, USA, *Geology*, 32(2), 141–144.
- Cashman, K. V., and S. M. McConnell (2005), Multiple levels of magma storage during the 1980 summer eruptions of Mount St. Helens, WA, *Bull. Volcanol.*, 68(1), 57–75.
- Cashman, K. V., and J. Taggart (1983), Petrologic monitoring of 1981 and 1982 eruptive products from Mount St. Helens, *Science*, 221(4618), 1385–1387.
- Chakraborty, P., G. Gioia, and S. Kieffer (2006), Volcán Reventador's unusual umbrella, *Geophys. Res. Lett.*, 33, L05313, doi:10.1029/2005GL024915.
- Cornell, W., S. Carey, and H. Sigurdsson (1983), Computer simulation of transport and deposition of the Campanian Y-5 ash, *J. Volcanol. Geotherm. Res.*, 17(1–4), 89–109.
- Costa, A., A. Folch, and G. Macedonio (2010), A model for wet aggregation of ash particles in volcanic plumes and clouds: 1. Theoretical formulation, *J. Geophys. Res.*, 115, B09201, doi:10.1029/2009JB007175.
- Criswell, C. W. (1987), Chronology and pyroclastic stratigraphy of the May 18, 1980, eruption of Mount St. Helens, Washington, *J. Geophys. Res.*, 92(B10), 10,237–10,266, doi:10.1029/JB092iB10p10237.
- Degruyter, W., and C. Bonadonna (2012), Improving on mass flow rate estimates of volcanic eruptions, *Geophys. Res. Lett.*, 39, L16308, doi:10.1029/2012GL052566.
- Druitt, T. H. (1992), Emplacement of the 18 May 1980 lateral blast deposit ENE of Mount St. Helens, Washington, *Bull. Volcanol.*, 54(7), 554–572.
- Dufek, J., and M. Manga (2008), In situ production of ash in pyroclastic flows, *J. Geophys. Res.*, 113, B09207, doi:10.1029/2007JB005555.
- Durant, A. J. (2015), RESEARCH FOCUS: Toward a realistic formulation of fine-ash lifetime in volcanic clouds, *Geology*, 43(3), 271–272.
- Durant, A. J., and W. I. Rose (2009), Sedimentological constraints on hydrometeor-enhanced particle deposition: 1992 eruptions of Crater Peak, Alaska, *J. Volcanol. Geotherm. Res.*, 186(1–2), 40–59.
- Durant, A. J., R. A. Shaw, W. I. Rose, Y. Mi, and G. G. J. Ernst (2008), Ice nucleation and overseeding of ice in volcanic clouds, *J. Geophys. Res.*, 113, D09206, doi:10.1029/2007JD009064.
- Durant, A. J., W. I. Rose, A. M. Sarna-Wojcicki, S. Carey, and A. C. M. Volentik (2009), Hydrometeor-enhanced tephra sedimentation: Constraints from the 18 May 1980 eruption of Mount St. Helens, *J. Geophys. Res.*, 114, B03204, doi:10.1029/2008JB005756.
- Engwell, S. L., J. Eychenne, S. Wulf, and M. de Micheli Vitturi (2014a), The characteristics of co-ignimbrite deposits and inferences for their formation, In: AGU (Editor), Abstract V21B-4757 presented at 2014a AGU Fall Meeting, San Francisco, Calif.

- Engwell, S. L., R. S. J. Sparks, and S. Carey (2014b), *Physical Characteristics of Tephra Layers in the Deep Sea Realm: The Campanian Ignimbrite Eruption*, *Geol. Soc. London Spec. Publ.*, vol. 398.
- Esposti Ongaro, T., C. Widiwijayanti, A. B. Clarke, B. Voight, and A. Neri (2011), Multiphase-flow numerical modeling of the 18 May 1980 lateral blast at Mount St. Helens, USA, *Geology*, *39*(6), 535–538.
- Eychenne, J., J.-L. Pennec, L. Troncoso, M. Gouhier, and J.-M. Nedelec (2012), Causes and consequences of bimodal grain-size distribution of tephra fall deposited during the August 2006 Tungurahua eruption (Ecuador), *Bull. Volcanol.*, *74*(1), 187–205.
- Farlow, N. H., V. R. Oberbeck, K. G. Snetsinger, G. V. Ferry, G. Polkowski, and D. M. Hayes (1981), Size distributions and mineralogy of ash particles in the stratosphere from eruptions of Mount St. Helens, *Science*, *211*(4484), 832–834.
- Fero, J., S. N. Carey, and J. T. Merrill (2008), Simulation of the 1980 eruption of Mount St. Helens using the ash-tracking model PUFF, *J. Volcanol. Geotherm. Res.*, *175*(3), 355–366.
- Fisher, R. (1964), Maximum size, median diameter, and sorting of tephra, *J. Geophys. Res.*, *69*(2), 341–355, doi:10.1029/JZ069i002p00341.
- Flentje, H., H. Claude, T. Elste, S. Gilge, U. Köhler, C. Plass-Dülmer, W. Steinbrecht, W. Thomas, A. Werner, and W. Fricke (2010), The Eyjafjallajökull eruption in April 2010—Detection of volcanic plume using in-situ measurements, ozone sondes and lidar-ceilometer profiles, *Atmos. Chem. Phys.*, *10*(20), 10,085–10,092.
- Folch, A., A. Costa, A. Durant, and G. Macedonio (2010), A model for wet aggregation of ash particles in volcanic plumes and clouds: 2. Model application, *J. Geophys. Res.*, *115*, B09202, doi:10.1029/2009JB007176.
- Folk, R. L. (1966), A review of grain-size parameters, *Sedimentology*, *6*, 73–93.
- Folk, R. L., and W. C. Ward (1957), Brazos River Bar: A study of the significance of grain size parameters, *J. Sediment. Petrol.*, *27*, 3–26.
- Genareau, K., G. Mulukutla, A. Proussevitch, A. Durant, W. Rose, and D. Sahagian (2013), The size range of bubbles that produce ash during explosive volcanic eruptions, *J. Appl. Volcanol.*, *2*(4), doi:10.1186/2191-5040-2-4.
- Gilbert, J. S., and S. J. Lane (1994), The origin of accretionary lapilli, *Bull. Volcanol.*, *56*(5), 398–411.
- Gislason, S. R., et al. (2011), Characterization of Eyjafjallajökull volcanic ash particles and a protocol for rapid risk assessment, *Proc. Natl. Acad. Sci. U.S.A.*, *108*(18), 7307–7312.
- Glicken, H. (1990), The rockslide—Debris avalanche of the May 18, 1980, eruption of Mount St. Helens—10th anniversary perspectives, *Geosci. Canada*, *17*, 150–153.
- Guéhenneux, Y., M. Gouhier, and P. Labazuy (2015), Improved space borne detection of volcanic ash for real-time monitoring using 3-Band method, *J. Volcanol. Geotherm. Res.*, *293*, 25–45.
- Harris, D. M., W. I. Rose, R. Roe, and M. R. Thompson (1981), *Radar Observations of Ash Eruptions*, *U.S. Geol. Surv. Prof. Pap.*, vol. 1250, pp. 323–334.
- Hobbs, P. V., L. F. Radke, M. W. Eltgroth, and D. A. Hegg (1981), Airborne studies of the emissions from the volcanic eruptions of Mount St. Helens, *Science*, *211*, 816–818.
- Hobbs, P. V., J. P. Tuell, D. A. Hegg, L. F. Radke, and M. W. Eltgroth (1982), Particles and gases in the emissions from the 1980–1981 volcanic eruptions of Mount St. Helens, *J. Geophys. Res.*, *87*(C13), 11,062–11,086, doi:10.1029/JC087iC13p11062.
- Hoblitt, R. P. (2000), Was the 18 May 1980 lateral blast at Mt St Helens the product of two explosions?, *Philos. Trans. R. Soc. London*, *358*, 1639–1661.
- Hoblitt, R. P., and R. S. Harmon (1993), Bimodal density distribution of cryptodome dacite from the 1980 eruption of Mount St. Helens, Washington, *Bull. Volcanol.*, *55*, 421–437.
- Hoblitt, R. P., C. D. Miller, and J. W. Vallance (1981), *Origin and Stratigraphy of the Deposit Produced by the May 18 Directed Blast*, *U.S. Geol. Surv. Prof. Pap.*, vol. 1250, pp. 401–420.
- Holasek, R. E., and S. Self (1995), GOES weather satellite observations and measurements of the May 18, 1980, Mount St. Helens eruption, *J. Geophys. Res.*, *100*(B5), 8469–8487, doi:10.1029/94JB03137.
- Hooper, P. R., I. W. Herrick, E. R. Laskowski, and C. R. Knowles (1980), Composition of the Mount St. Helens ashfall in the Moscow–Pullman area on 18 May 1980, *Science*, *209*(4461), 1125–1126.
- Hopkins, A. T., and C. J. Bridgman (1985), A volcanic ash transport model and analysis of Mount St. Helens ashfall, *J. Geophys. Res.*, *90*(D6), 10,620–10,630, doi:10.1029/JD090iD06p10620.
- Ikramuddin, M., S. J. M. Digby, and A. R. Buehler (1982), Chemical composition of the Mount St. Helens ash from the 18 May eruption, in *Proceedings, Mount St. Helens: One Year Later*, edited by S. A. C. Keller, pp. 27–32, Eastern Washington Univ. Press, Cheney.
- Johnson, B., et al. (2012), In situ observations of volcanic ash clouds from the FAAM aircraft during the eruption of Eyjafjallajökull in 2010, *J. Geophys. Res.*, *117*, D00U24, doi:10.1029/2011JD016760.
- Kaminski, E., and C. Jaupart (1998), The size distribution of pyroclasts and the fragmentation sequence in explosive volcanic eruptions, *J. Geophys. Res.*, *103*(B12), 29,759–29,779, doi:10.1029/98JB02795.
- Kieffer, S. W. (1981), *Fluid Dynamics of the May 18 Blast at Mount St. Helens*, *U.S. Geol. Surv. Prof. Pap.*, vol. 1250, pp. 379–400.
- Klug, C., and K. V. Cashman (1994), Vesiculation of May 18, 1980, Mount St. Helens magma, *Geology*, *22*, 468–472.
- Koyaguchi, T. (1994), Grain-size variation of tephra derived from volcanic umbrella clouds, *Bull. Volcanol.*, *56*(1), 1–9.
- Kueppers, U., D. Perugini, and D. B. Dingwell (2006), “Explosive energy” during volcanic eruptions from fractal analysis of pyroclasts, *Earth Planet. Sci. Lett.*, *248*(3–4), 800–807.
- Kueppers, U., C. Cimarelli, K.-U. Hess, J. Taddeucci, F. Wadsworth, and D. Dingwell (2014), The thermal stability of Eyjafjallajökull ash versus turbine ingestion test sands, *J. Appl. Volcanol.*, *3*(1), 4.
- Kuntz, M. A., P. D. Rowley, N. S. Macleod, R. L. Reynolds, L. A. McBroome, A. M. Kaplan, and D. J. Lidke (1981), *Petrography and Particle-Size Distribution of Pyroclastic-Flow, Ash-Cloud, and Surge Deposits*, *U.S. Geol. Surv. Prof. Pap.*, vol. 1250, pp. 525–540.
- Labazuy, P., M. Gouhier, A. Harris, Y. Guéhenneux, M. Hervo, J. C. Bergès, P. Fréville, P. Cacault, and S. Rivet (2012), Near real-time monitoring of the April–May 2010 Eyjafjallajökull ash cloud: An example of a web-based, satellite data-driven, reporting system, *Int. J. Environ. Pollut.*, *48*(1), 262–272.
- Mackie, S., and M. Watson (2014), Probabilistic detection of volcanic ash using a Bayesian approach, *J. Geophys. Res. Atmos.*, *119*, 2409–2428, doi:10.1002/2013JD021077.
- Manga, M., A. Patel, and J. Dufek (2011), Rounding of pumice clasts during transport: Field measurements and laboratory studies, *Bull. Volcanol.*, *73*(3), 321–333.
- Manzella, I., C. Bonadonna, J. C. Phillips, and H. Monnard (2015), The role of gravitational instabilities in deposition of volcanic ash, *Geology*, *43*, 211–214.
- Master, L. G., et al. (2009), A multidisciplinary effort to assign realistic source parameters to models of volcanic ash-cloud transport and dispersion during eruptions, *J. Volcanol. Geotherm. Res.*, *186*(1–2), 10–21.
- Master, L. G., A. R. Van Eaton, and J. B. Lowenstern (2014), Modeling ash fall distribution from a Yellowstone supereruption, *Geochem. Geophys. Geosyst.*, *15*, 3459–3475, doi:10.1002/2014GC005469.

- Moore, J. G., and C. J. Rice (1984), Chronology and character of the May 18, 1980, explosive eruptions of Mount St. Helens, in *Explosive Volcanism, Inception, Evolution, and Hazards*, pp. 133–142, Natl. Acad. Sci. Press, Washington, D. C.
- Moore, J. G., and T. W. Sisson (1981), *Deposits and Effects of the May 18 Pyroclastic Surge, U.S. Geol. Surv. Prof. Pap.*, vol. 1250, pp. 421–438.
- Muir, D. D., J. D. Blundy, and A. C. Rust (2012), Multiphase petrography of volcanic rocks using element maps: A method applied to Mount St. Helens, 1980–2005, *Bull. Volcanol.*, *74*(5), 1101–1120.
- Pouget, S., M. Bursik, P. Webley, J. Dehn, and M. Pavlonis (2013), Estimation of eruption source parameters from umbrella cloud or downwind plume growth rate, *J. Volcanol. Geotherm. Res.*, *258*, 100–112.
- Pyle, D. M. (1989), The thickness, volume and grain size of tephra fall deposits, *Bull. Volcanol.*, *51*, 1–15.
- Quinn, R. R. (1982), Variations in atmospheric circulation, Mount St. Helens eruption, 1980, in *Proceedings: Mount St. Helens, One Year Later*, edited by S. A. C. Keller, pp. 71–78, Eastren Washington Univ. Press, Cheney.
- Rice, C. J. (1981), Satellite observations of the Mount St. Helens eruption of 18 May 1980, *Proc. SPIE Int. Soc. Opt. Eng.*, *278*, 23–31.
- Rose, W., and A. Durant (2009), Fine ash content of explosive eruptions, *J. Volcanol. Geotherm. Res.*, *186*, 32–39.
- Rose, W., D. Harris, G. Heiken, A. Sarna-Wojcicki, and S. Self (1982), Volcanological description of the 18 May 1980 eruption of Mount St. Helens. Mount St. Helens eruptions of 1980: Atmospheric effects and potential climatic impact: 1–36.
- Rose, W. I. (1993), Comment on 'another look at the calculation of fallout tephra volumes' by Judy Fierstein and Manuel Nathenson, *Bull. Volcanol.*, *55*(5), 372–374.
- Rosenbaum, J. G., and R. B. Waitt (1981), *Summary of Eye-Witness Accounts of the May 18 Eruption, U.S. Geol. Surv. Prof. Pap.*, vol. 1250, pp. 53–68.
- Rowley, P. D., M. A. Kuntz, and N. S. Macleod (1981), *Pyroclastic-Flow Deposits, U.S. Geol. Surv. Prof. Pap.*, vol. 1250, pp. 489–512.
- Rust, A. C., and K. V. Cashman (2011), Permeability controls on expansion and size distributions of pyroclasts, *J. Geophys. Res.*, *116*, B11202, doi:10.1029/2011JB008494.
- Rutherford, M. J., H. Sigurdsson, S. Carey, and A. Davis (1985), The May 18, 1980, eruption of Mount St. Helens: 1. Melt composition and experimental phase equilibria, *J. Geophys. Res.*, *90*(B4), 2929–2947, doi:10.1029/JB090iB04p02929.
- Sarna-Wojcicki, A., S. Shipley, R. B. Waitt, D. Dzurisin, and S. Wood (1981), *Aerial Distribution, Thickness, Mass, Volume and Grain Size of Air-Fall Ash From the Six Major Eruptions of 1980, U.S. Geol. Surv. Prof. Pap.*, vol. 1250, pp. 577–600.
- Scandone, R., K. V. Cashman, and S. D. Malone (2007), Magma supply, magma ascent and the style of volcanic eruptions, *Earth Planet. Sci. Lett.*, *253*(3–4), 513–529.
- Scheidegger, K. F., A. N. Federman, and A. M. Tallman (1982), Compositional heterogeneity of tephra from the 1980 eruptions of Mount St. Helens, *J. Geophys. Res.*, *87*(B13), 10,861–10,881, doi:10.1029/JB087iB13p10861.
- Schultz, D. M., et al. (2006), The mysteries of mammatus clouds: Observations and formation mechanisms, *J. Atmos. Sci.*, *63*(10), 2409–2435.
- Schumacher, R. (1994), A reappraisal of Mount St. Helens' ash clusters—Depositional model from experimental observation, *J. Volcanol. Geotherm. Res.*, *59*(3), 253–260.
- Sorem, R. K. (1982), Volcanic ash clusters: Tephra rafts and scavengers, *J. Volcanol. Geotherm. Res.*, *13*(1–2), 63–71.
- Sparks, R. S. J., and T. C. Huang (1980), The volcanological significance of deep-sea ash layers associated with ignimbrites, *Geol. Mag.*, *117*, 425–436.
- Sparks, R. S. J., and G. P. L. Walker (1977), The significance of vitric-enriched air-fall ashes associated with crystal-enriched ignimbrites, *J. Volcanol. Geotherm. Res.*, *2*, 329–341.
- Sparks, R. S. J., S. Self, and G. P. L. Walker (1973), Products of ignimbrite eruptions, *Geology*, *1*(3), 115–118.
- Sparks, R. S. J., S. Brazier, T. C. Huang, and D. Muerdter (1984), Sedimentology of the Minoan deep-sea tephra layer in the Aegean and Eastern Mediterranean, *Mar. Geol.*, *54*, 131–167.
- Sparks, R. S. J., J. G. Moore, and C. J. Rice (1986), The initial giant umbrella cloud of the May 18th, 1980, explosive eruption of Mount St. Helens, *J. Volcanol. Geotherm. Res.*, *28*, 257–274.
- Sparks, R. S. J., M. I. Bursik, G. J. Ablay, R. M. E. Thomas, and S. N. Carey (1992), Sedimentation of tephra by volcanic plumes. Part 2: Controls on thickness and grain-size variations of tephra fall deposits, *Bull. Volcanol.*, *54*(8), 685–695.
- Sparks, R. S. J., M. I. Bursik, S. N. Carey, J. S. Gilbert, L. S. Glaze, H. Sigurdsson, and A. W. Woods (1997), *Volcanic Plumes*, John Wiley, Chichester.
- Stevenson, J. A., S. C. Millington, F. M. Beckett, G. T. Swindles, and T. Thordarson (2015), Big grains go far: Reconciling tephrochronology with atmospheric measurements of volcanic ash, *Atmos. Meas. Tech. Discuss.*, *8*(1), 65–120.
- Stohl, A., et al. (2011), Determination of time- and height-resolved volcanic ash emissions and their use for quantitative ash dispersion modeling: The 2010 Eyjafjallajökull eruption, *Atmos. Chem. Phys.*, *11*, 4333–4351.
- Stoiber, R. E., S. N. Williams, L. L. Malinconico Jr., D. A. Johnston, and T. J. Casadevall (1981), Mt. St. Helens: Evidence of increased magmatic gas component, *J. Volcanol. Geotherm. Res.*, *11*(2–4), 203–212.
- Taddeucci, J., and D. M. Palladino (2002), Particle size-density relationships in pyroclastic deposits: Inferences for emplacement processes, *Bull. Volcanol.*, *64*(3–4), 273–284.
- Van Eaton, A., J. Muirhead, C. N. Wilson, and C. Cimarelli (2012), Growth of volcanic ash aggregates in the presence of liquid water and ice: An experimental approach, *Bull. Volcanol.*, *74*(9), 1963–1984.
- Voight, B. (1981), *Time Scale for the First Moments of the May 18 Eruption, U.S. Geol. Surv. Prof. Pap.*, vol. 1250, pp. 69–86.
- Waitt, R. B. (2015), *In the Path of Destruction: Eyewitness Chronicles of Mount St. Helens*, 413 pp., Washington State Univ. Press, Pullman.
- Waitt, R. B., and D. Dzurisin (1981), *Proximal Air-Fall Deposits From the May 18 Eruption—Stratigraphy and Field Sedimentology, U.S. Geol. Surv. Prof. Pap.*, vol. 1250, pp. 601–616.
- Wiesner, M. G., A. Wetzel, S. G. Catane, E. L. Listanco, and H. T. Mirabueno (2004), Grain size, areal thickness distribution and controls on sedimentation of the 1991 Mount Pinatubo tephra layer in the South China Sea, *Bull. Volcanol.*, *66*(3), 226–242.
- Witham, C. S., M. C. Hort, R. Potts, R. Servranckx, P. Husson, and F. Bonnardot (2007), Comparison of VAAC atmospheric dispersion models using the 1 November 2004 Grimsvötn eruption, *Meteorol. Appl.*, *14*(1), 27–38.
- Wohletz, K. H., M. F. Sheridan, and W. K. Brown (1989), Particle size distributions and the sequential fragmentation/transport theory applied to volcanic ash, *J. Geophys. Res.*, *94*(B11), 15,703–15,721, doi:10.1029/JB094iB11p15703.
- Woodhouse, M. J., A. J. Hogg, J. C. Phillips, and R. S. J. Sparks (2013), Interaction between volcanic plumes and wind during the 2010 Eyjafjallajökull eruption, Iceland, *J. Geophys. Res. Solid Earth*, *118*, 92–109, doi:10.1029/2012JB009592.